

#### Journal of Stress Analysis

Vol. 8, No. 1, 2023-24, 19-26



ORIGINAL RESEARCH PAPER

# Experimental Study of the Strength and Residual Stresses of the Friction Stir Welding Process of Explosive-Welded Al1050/Al2024/Al1050

Mohammad Reza Aftabi, Mohammad Honarpisheh\*

Manufacturing Department, Faculty of Mechanical Engineering, University of Kashan, Kashan, Iran.

#### Article info

Article history: Received 30 January 2023 Received in revised form 06 July 2023 Accepted 22 August 2023

Keywords: Friction stir welding Residual stress Contour method Mechanical properties Al1050/Al2024/Al1050

#### Abstract

In this research, the distribution of the hardness and residual stress in the joining of three layers of explosion-welded Al1050/Al2024/Al1050 aluminum alloy sheets, which were friction stir welded, was investigated. The rotational speed and traverse speed parameters were determined by trial and error in order to achieve a weld without cracks and holes. Due to the selection of steel tools with a shoulder diameter of 20mm and an incomplete conical pin with a large diameter of 4mm, only the desired welds were made at a rotational speed of 710rpm, a forward speed of 16mm/min and 20mm/min, a rotational speed of 1120rpm, and a transverse speed of 20mm/min. In other cases, the welding has defects or low surface quality. To check the residual stress, the contour method, which is one of the new destructive methods, was used. By examining the obtained results, it was found that the residual stress in the center of the part (welded zone) was tensile, and it was compressive at the edges of the part along the thickness. Considering the yield strength of the base metal, which was about 205 MPa, and the highest value of residual stress, which was about 35MPa, at a rotational speed of 710rpm with a transverse speed of 20mm/min, the highest residual stress was about 17% of the yield strength of the base metal.

#### 1. Introduction

Aluminum alloys with high strength-to-weight ratio, formability, and high corrosion resistance are widely used in aerospace, shipbuilding, and railway industries. With the growth of aluminum consumption in various industries, the connection of aluminum alloys becomes more important. In the past, due to the difficulty in creating high-strength, fatigue- and corrosion-resistant welds in aluminum alloys (series 2 and 7) used in the aerospace industry, the use of welding was limited in these industries. These types of aluminum alloys are non-weldable, due to the porous structure as well as

the loss of mechanical properties in the melting zone, the welding quality is very poor compared to the base metal. These factors have made it uninteresting to join alloys by conventional welding processes. Some aluminum alloys can be joined by resistance welding, but preparing their surface for welding is expensive because oxidation of the surface during the process is a major limitation. On the other hand, in recent years, the use of solid state welding methods for metal alloys, especially aluminum, has grown significantly. Friction stir welding (FSW) is one of the solid state welding methods used for welding metal alloys, mainly aluminum

\*Corresponding author: M. Honarpisheh (Assistant Professor) E-mail address: honarpishe@kashanu.ac.ir

doi 10.22084/JRSTAN.2024.28087.1246

ISSN: 2588-2597



and magnesium. This process was invented in 1991 by the UK TWI Welding Institute [1]. Sonne et al. [2] in 2013 investigated the effects of work hardening and thermal softening laws on the simulation of residual stress in FSW of 2024 aluminum alloy. The effect of working conditions in cold welding did not have any effect on the residual stress, while in hot welding conditions, the reduction of the yield stress had a significant effect on the residual stress, especially near the weld line. Jafari et al. [3] studied mechanical properties and residual stress variations of friction stir welded dissimilar Al-6061-T6 and Al-7075-T6 alloys. Alinaghian et al. [4] used the ultrasonic vibrations in FSW of Al 6061-T6. They investigated the residual stress, mechanical properties and macrostructures of the welded samples. Cavalier et al. [5] in 2005 investigated the mechanical properties of non-homogeneous 2024-7075 aluminum alloy with a thickness of 2.5mm in FSW. According to the evaluations of the tensile test, the results showed that there was an increase in the longitudinal strength of the sample. Also, the fatigue test showed that the fatigue life of the 2024 alloy increased and that the fatigue life of the 7075 alloy decreased. Aonuma et al. [6] in 2011 studied the FSW of 2024 and 7075 aluminums to titanium alloys. The weldability of alloy 2024 to titanium was better than alloy 7075 and it had higher tensile strength. Also, the welding speed had a direct effect on the tensile strength in such a way that with the increase of the welding speed, the tensile strength of the aluminum-titanium alloy connection increased as well, and the hardness of the base metals also had an effect on the weldability of the aluminum-titanium alloys. By examining the welding surface by means of XRD, they observed the intermetallic compound of TiAl<sub>3</sub> in this area, and this intermetallic compound was effective on the tensile strength. Prime et al. [7] in 2006 measured the residual stress in non-homogeneous aluminum alloys 7050-2024 in FSW by contour method. The results obtained from the measurement of residual stress in FSW of 7050 and 2024 aluminum alloy plates with a thickness of 25.4mm were as follows: the maximum stress was about 43MPa, which was less than 20% of the final strength of the material. To remove a piece of test specimen from a larger piece in order to maintain the principal residual stresses in the middle of the length of the specimen, the length had to be 2 to 3 times the specified distance. Alinaghian et al. [8] used BM-UAFSW (bending mode ultrasonic-assisted FSW) to investigate the residual stress variations at various vibration amplitudes. They used the contour method to measure the longitudinal residual stress of Al-6061-T6 plates with thicknesses of 3mm and 5mm. Eivani etcal. [9] presented a new approach to measure the residual stress of AZ91 Mg alloy after the FSW process. They used combined smoothed particle hydrodynamics/neuro-fuzzy computations and ultrasonic testing. Salvati et al. [10] studied the residual stress field in FSW butt joint aluminum alloy using X-ray powder diffraction and ion beam and digital image correlation (FIB-DIC) methods. Delijaicov et al. [11] measured the residual stress of dissimilar joints of Al-7181-T7651 and Al-7475-T7351. They used the integral method in incremental hole drilling. Their results showed the positive longitudinal residual stresses. Salloomi and Al-Sumaidae [12] used coupled Eulerian— Lagrangian (CEL) modeling to analyze thermal and residual stress in friction stir welding of Al-6061-T6 and Al-2024-T3 alloys. Kaid et al. [13] analyzed the residual stress of 6061-T6 aluminum alloy by numerical modeling. They used the ANSYS software and compare their results with experimental data. Zhan et al. [14] used laser ultrasonic technology to measure the residual stress of Al-7075 after the FSW process. They found that the residual stress on the advancing side was greater than that on the retreating side. Liu et al. [15] measured the 3D residual stress field of FSWed thick plates Al-6005-T6 by neutron diffraction.

It is usually difficult and sometimes impossible to join aluminum sheets with conventional welding methods. Methods such as explosive welding of aluminum sheets are used for welding two surfaces of sheets, and friction stir welding is used to join sheet butts to each other. In this study, the friction stir welding process was performed on the explosive welded sheets. Therefore, the surface of Al1050 and Al2024 alloys were joined together by explosive welding process. Then, the FSW process was used for butt welding process. Also, the measurement of residual stress after FSW has not been reported. Therefore, in this research, the FSW process of explosive-welded Al1050/Al2024/Al1050 sheets and the measurement of residual stress in these joints were evaluated.

#### 2. Research Method

The material of the work piece used in this research was three-layer explosion-welded aluminum with an alloy order of Al1050Al/Al2024/Al1050 with a thickness of 5mm. The desired three-layer sheet was cut in dimensions of  $100 \times 45$ mm and prepared for testing. Also, in order to perform welding operations, a tool with a pin diameter of 4mm, a pin height of 4.7mm, and a shoulder diameter of 20mm was used. The parameters investigated in this study include rotational speed and transverse speed. According to the applied variables, the number of tests performed and their details are given in Table 1.

After preparing the samples and determining the test conditions, such as determining the parameters and constraints used (Fig. 1a) as well as the welding machine, the operation was performed.

The first step in examining welding samples is ten-

sile testing. For this purpose, it is necessary to prepare the samples for the tensile test. The samples were prepared according to ASTM E8 standard [16] to perform the tensile strength test. The dimensions of the tensile test specimen are displayed in Fig. 2. For repeatability, two tests were performed for each condi

Table 1
Design of experiment.

No.	Rotational	Transverse
	speed (rpm)	speed (mm/min)
1	710	16
2	710	20
3	900	16
4	900	20
5	900	25
6	1120	16
7	1120	20
8	1120	25
9	1400	16
10	1400	20
11	1400	25



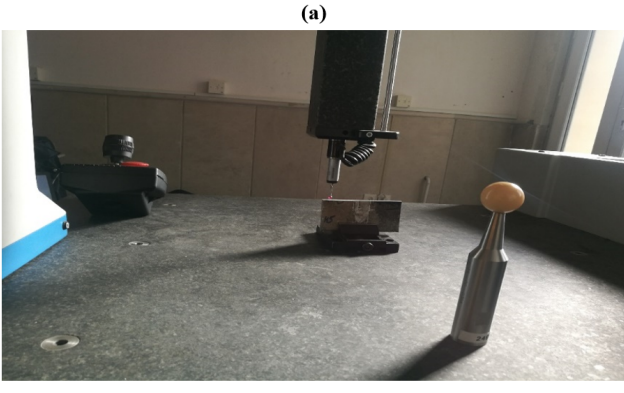


**Fig. 1.** a) Schematic of FSW process b) Measuring the residual stress by a coordinate-measuring machine.

(b)

After performing the tensile test and determining the acceptable samples, the residual stresses in the samples were checked. The contour method is one of the newest residual stress measurement methods, which was first proposed by Prime in 2000 [17]. For this purpose, the parts were cut with a wire cutter, which had special conditions so that residual stress would not be created in the samples during the operation. These conditions include: disposable wirecut wire, brass wire material, wire diameter less than 0.25mm, cutting in finishing mode and cutting speed less than 40 square mm/min.

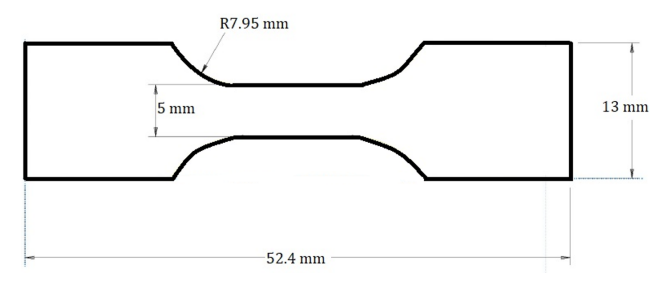


Fig. 2. Dimensions of the tensile test specimen.

After cutting the piece by wirecut, the peaks and valleys created on the cutting surface due to the release of residual stress on the surface were measured by a coordinate-measuring machine (CMM) (Fig. 1b). Then, after the removing the outlier data, a cloud of points or an equation was obtained from the resulting points in MATLAB software. The resulting point cloud must be the best point cloud passing through the points. After preparing the necessary information, the analysis process was done in ABAQUS software. To do this, a 3D model of the cutting surface was created. The cutting surface was modeled as a flat surface and the contour of the measured surface was applied as boundary conditions to the modeled surface. The C3D8R elements were used for meshing the model. By creating a partition in the model, the size of the elements on the cut surface was considered to be 0.5×0.5mm, similar to what was considered for measuring the surface contour and the rest of the model with elements, the coarse particles were gridded. The microhardness of the samples was measured in such a way that after measuring the residual stresses on the surface of the samples.

#### 3. Result and Discussion

In this part, the measurement of the strength of the created weld bond and the residual stresses created in the samples are discussed. According to the results, all the variables used did not provide the desired results. This was based on the past research on each of these alloys separately; however, this type of alloy material had never been investigated. Thus, a suitable range for this type of alloy could be considered as the best range for obtaining a better weld, which was the result of the research. Considering this range, the suitable rotational speed was between 710 and 1120rpm,

and also better results were obtained in the traverse speeds of 16 and 20mm/min. At a rotational speed of 1400rpm, the desired welding speed was not achieved and there were visible defects. It is also worth mentioning that one sample was also made with a rotational speed of 560rpm and a speed of 20mm/min, which required heat. However, welding is not achieved at this rotational speed and causes the sample to crumble during welding. According to the test conditions, the results of the samples are given in Fig. 3 and Table 2.

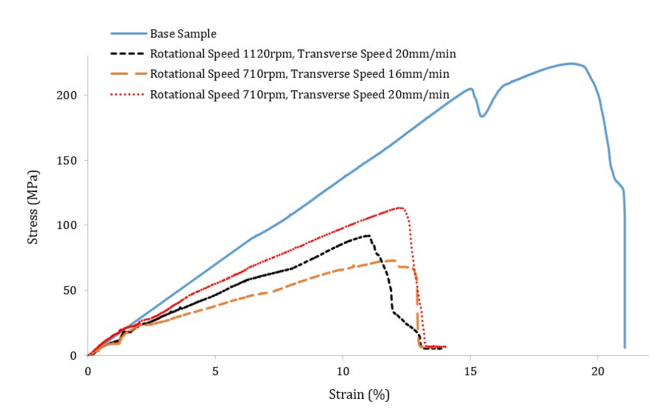


**Fig. 3.** Tensile test results for the base sample and FSWed samples.

**Table 2** Effects of rotational speed and transverse speed on yield strength of samples.

No.	Rotational	Transverse	Yield
	speed (rpm)	speed (mm/min)	strength (MPa)
1	710	16	48± <b>1</b>
2	710	20	$63 \pm 0.4$
3	900	16	$18.7 \pm 0.3$
4	900	20	$24.2 \pm 0.6$
5	900	25	$21.7 \pm 0.6$
6	1120	16	$12 \pm 0.7$
7	1120	20	$37 \pm 0.5$
8	1120	25	$18.7 \pm 0.6$
9	1400	16	$15.6 \pm 0.4$
10	1400	20	$26.3 \pm 0.4$
11	1400	25	$12.4 \pm 0.5$

According to Fig. 3, at the rotational speed of 710rpm with the increase of the traverse speed from 16 to 20mm/min, the weld yield strength increased. This can be due to the high input heat generated at this rotational speed. Also, at the rotational speed of 900rpm, the strength increased by changing the welding speed from 16 to 20mm/min, which can be caused by the improvement of the input heat in the interaction with the disruption of the materials, that is, at the speed of 16mm/min.By increasing the traverse speed from 20 to 25mm, the yield strength decreased, which in this case, contrary to the first case, the unfavorable disruption of the materials reduced the yield strength. However, the yield strength at the welding speed of 25mm/min was

better than 16mm/min, indicating the better interaction of these two parameters, i.e. heat input and material consumption during welding. But it is expected that the yield strength will continue to decrease with the increase of welding speed. By comparing the two speeds of 16 and 20mm/min, the results at the rotational speed of 1120 rpm show that the excessive input heat at a speed of 16mm/min caused the yield strength to decrease. Also, by increasing the speed from 20 to 25mm/min, the yield strength decreased, which could be due to the unfavorable mixing of the materials and the formation of welds with structural and appearance defects. Also, based on the comparison of speed of 16 and 25mm/min, we found that the interaction of the two parameters of input heat and the material disturbance at the speed of 25mm/min was better, and the weld with better yield strength was achieved. However, it is predicted that with a further increase in the welding speed, the yield strength of the welds would follow a downward trend as well. Also, the results at the rotational speed of 1400 increased the yield strength by increasing the traverse speed from 16 to 20mm/min, which can be as the result of the excessive heat input. Moreover, by increasing the speed from 20 to 25mm/min, the strength of the weld decreased. Due to improper mixing of the materials, which causes the application of insufficient temperature during welding, the strength of the welds decreased. Also, by comparing two speeds of 16 and 25mm/min, it is also evident that the interaction of the two parameters of input heat and material consumption was better at the speed of 16mm/min because it achieved better yield strength; therefore, it is predicted that increasing the welding speed (advance) would result in reduced yield strength. The results of changing the welding speed parameter (advance) in each rotational speed were fully described. Now, according to the graphs, it can be seen that as the rotational speed increased, the process of changing the yield strength decreased. This can be due to the increase or even decrease of the input heat, which occurs relatively according to the welding speeds, i.e. if the rotational speed and the traverse speed are both high, the input heat is insufficient, indicating the greater effect of the traverse speed or interference. The material is desirable and if the rotational speed is high and the traverse speed is low, excessive input heat would be produced. Fig. 4 demonstrates the result of the analysis done in Minitab, and it shows the interaction of the two parameters, rotational speed and forward speed.

Fig. 5 displays the results about microhardness of the samples. The measurement was performed according ASTM E92-17. The micro-hardness of the samples was marked with five points in such a way that three points of the microhardness of the layers and the remaining two points of the microhardness of the boundary between the two layers were measured.

According to the results, it is clear that the micro-

hardness is higher in the boundary between the layers. Also, the microhardness in the middle of the piece has the lowest value, which was observed in all cases and all samples followed a similar trend.

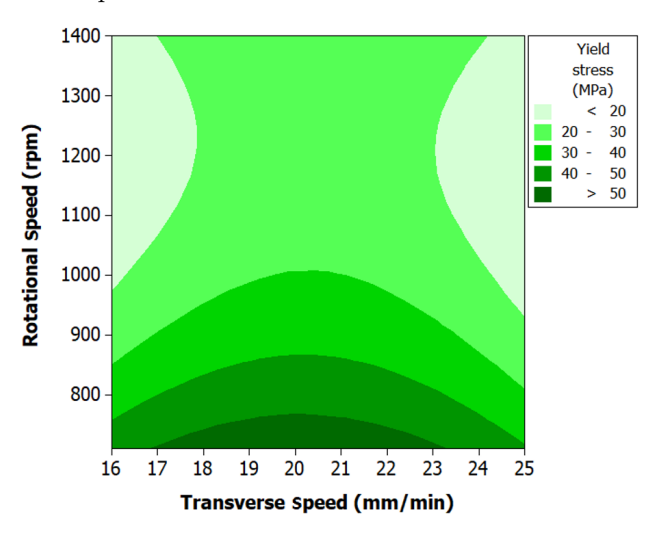


Fig. 4. Effects of transverse speed and rotational speed on the yield stress of samples.

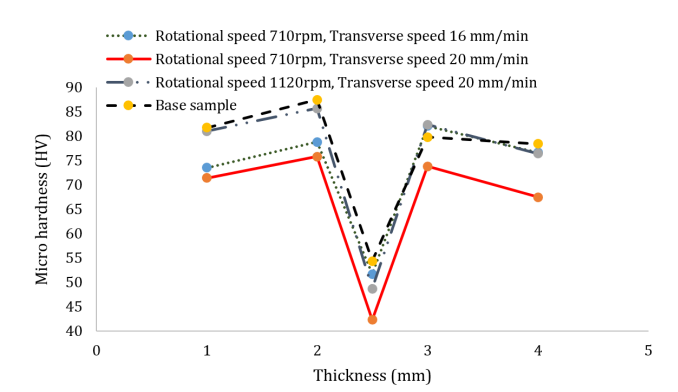
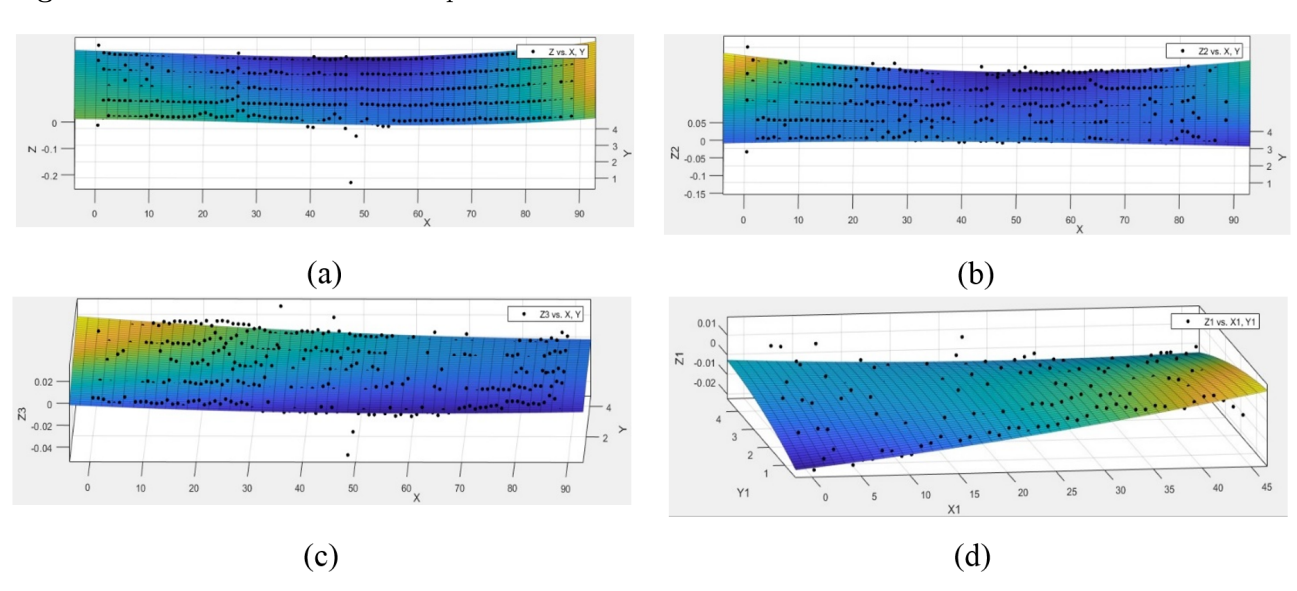


Fig. 5. Microhardness results of samples.



**Fig. 6.** Cloud points of cut surfaces at rotational speed and transverse speed a) 1120-20 b) 710-16 c) 710-20 d) as received.

It is also found from the results that the lowest hardness value in the samples varies between 45 and 55 Vickers and that the highest hardness value in the samples varies between 70 and 85 Vickers. Therefore, according to these cases, an approximate appropriate range was considered to determine the two parameters of rotational speed and forward speed. However, according to the resulting yield strengths, only three samples of these tests obtained more acceptable results; hence, only the three mentioned samples were used to measure the residual stresses.

To measure the residual stresses, we first need the super points of the surfaces or the plane equation. The point clouds of the surfaces are given in Fig. 6.

After defining the super points of the surfaces and obtaining the equation of the surfaces, we considered the resulting equation as the displacement boundary condition in the modeling. The stress contours of the surfaces are specified in Fig. 7.

After determining the stress contour, two paths were considered in the direction of thickness and length. The results are given in Figs. 8 to 11.

The diagrams above show the residual stresses created along the thickness (transverse) in three welding samples and the control sample. It can be seen from Fig. 8 that there are tensile residual stresses in the middle of the workpiece in all four samples. Therefore, due to the absence of melting, the intensity of heat, which is one of the main factors causing residual stresses, was reduced. On the other hand, due to the doughy nature of the mixing zone, the material had a greater tendency to release residual stresses. This phenomenon happens because of the equilibrium nature of cooling. They released larger amounts of stress compared to melting methods, and this is caused by the lower cooling thermal gradient.

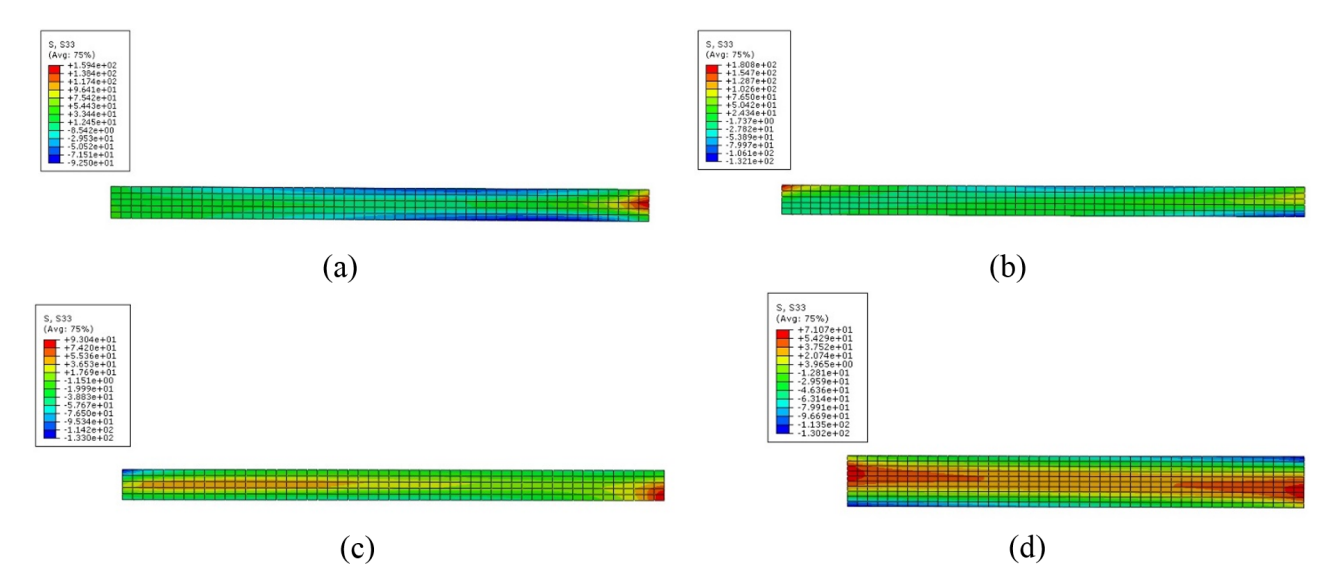


Fig. 7. Residual stress contour in levels a) 1120-20 b) 710-16 c) 710-20 d) as received.

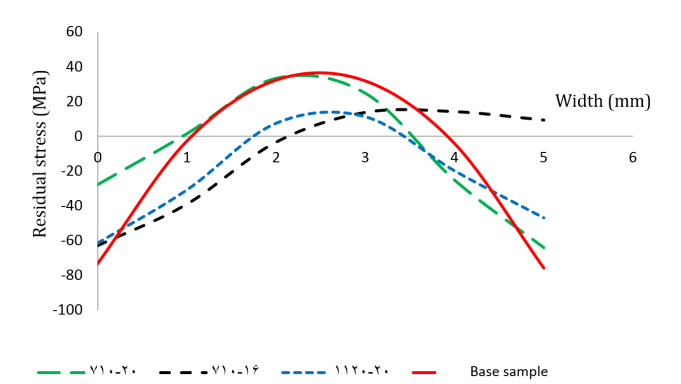


Fig. 8. Transverse residual stress results.

Given the fact that the materials included two different alloys with different mechanical and thermal properties, the thermal slopes were also different from one another. Also, by comparing the values of the graphs, it is clear that the effects of changes in rotational speed were slightly greater than the effects of changes in traverse speed. The diagram below compares two samples at a rotational speed of 710rpm.

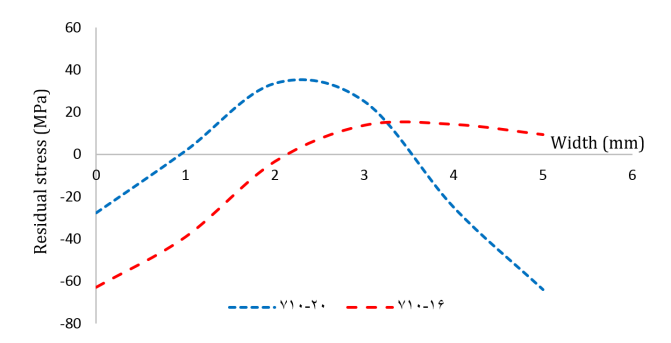


Fig. 9. Comparing the results of samples with a rotational speed of 710rpm.

According to the diagram of the residual stresses created in two samples at the rotational speed of 710rpm and the traverse speeds of 16 and 20mm/min, it is evident that tensile stresses were created in the middle of the workpiece, and on the contrary to predictions, the value of tensile stresses created in the advance of 20 was more than 16, which is due to the fact that the rate of strain created on the connection increased with the increase in the traverse speed. The graph below compares two samples at a forward speed of 20mm/min.

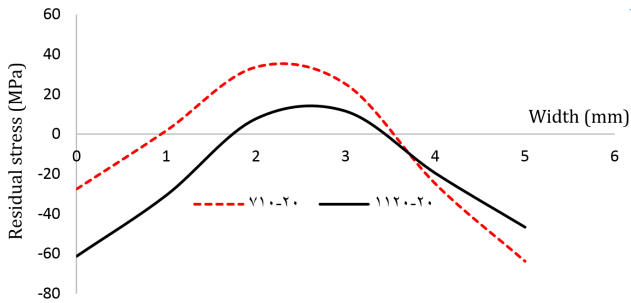


Fig. 10. Comparison of the results of the samples with the transverse speed of 20mm/min.

The above diagram compares two welding samples at rotational speeds of 710 and 1120rpm and traverse speed of 20mm/min. What is clear is the presence of tensile residual stresses in the middle of the samples. Furthermore, the values of these tensions were less than 710 at the rotational speed of 1120, on the contrary to our expectations. At lower rotational speeds, the effectiveness of increasing the tension decreased compared to the advancing speed. At lower rotational speeds (710rpm), increasing the traverse speed had a greater increasing effect on the residual stress in welding,; therefore, according to the reasons mentioned, the residual stress at the rotational speed of 710rpm was higher than that at 1120rpm.

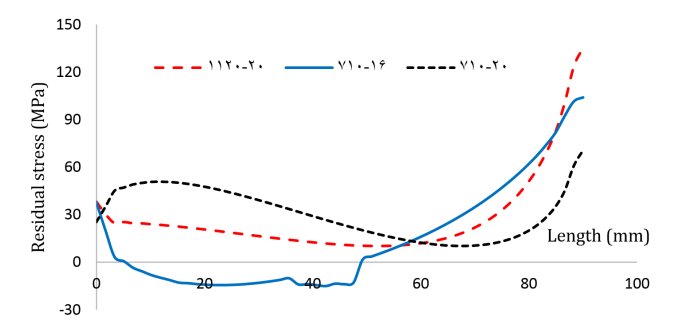


Fig. 11. Comparing the results of longitudinal residual stress.

The above diagram shows the residual stresses created in the longitudinal direction. According to the diagrams in different conditions, it can be found that with the increase in the traverse speed, there was an increase in the residual stresses, which is due to the increase in speed and, as a result, the increase in heat of the sample. Also, by increasing the rotational speed at the same forward speed, despite the presence of more heat at the rotational speed of 1120rpm, there was a reduction in residual stresses. This behavior is related to the influence of the rotational speed on the heat input and the temperature distribution on the joint. Therefore, increasing the rotational speed causes for a higher temperature and more uniform thermal distribution and reducing temperature gradients. As a result, less deformation or less plastic strain rate and less residual stresses were observed in welded plates with a higher rotational speed, which means that the effect of plastic strain rate was more than the increase in heat caused by the increase in rotational speed. It can also be seen that at the rotational speed of 710rpm and the advancing speed of 16mm/min, compressive residual stresses were created in the sample, which can be due to the low heat factor in the sample and the lower rotational speed. Additionally, the maximum longitudinal residual stress increased for higher rotational speeds of the tool. As previously reported in [18], the peak of tensile residual stresses was found in the longitudinal direction. In another research [19], the tensile residual was observed in the longitudinal direction with peak values of about 130MPa in the FSW process of aluminum alloy. As it can be seen in other works [20, 21], the residual stress in the welding zone has its maximum value, which increases with the increase in rotational speed.

#### 4. Conclusions

In this research, the effects of rotational speed and tool traverse speed in FSW of three-layer aluminum sheets with other parameters being constant were investigated. The results were checked at four rotational speeds of 710, 900, 1120, and 1400rpm and with traverse speeds of 16, 20, and 25mm/min as follows:

- As the advancing speed increases, the value of residual stress increases due to the increase in the strain rate.
- As the rotational speed increases, the value of residual stress increases due to the increase in temperature.
- At a rotational speed of 710rpm, with an increase in traverse speed from 16 to 20mm/min, the growth of residual stresses is higher than that at a rotational speed of 1120rpm, indicating that the effect of strain rate prevails at lower rotational speeds and the effect of heat prevails at higher speeds.
- At the rotational speed of 1400, the weld had visible defects and the weld surface was completely unacceptable.

#### References

- W., Thomas, International Patent Application No. PCT/GB92, GB Patent Application No. 9125978, (1991).
- [2] M.R. Sonne, C.C. Tutum, J.H. Hattel, A. Simar, B. De Meester, The effect of hardening laws and thermal softening on modeling residual stresses in FSW of aluminum alloy 2024-T3, J. Mater. Process. Technol., 213(3) (2013) 477-486.
- [3] H. Jafari, H. Mansouri, M. Honarpisheh, Investigation of residual stress distribution of dissimilar Al-7075-T6 and Al-6061-T6 in the friction stir welding process strengthened with SiO2 nanoparticles, J. Manuf. Process., 43 (2019) 145-153.
- [4] I. Alinaghian, S. Amini, M. Honarpisheh, Residual stress, tensile strength, and macrostructure investigations on ultrasonic assisted friction stir welding of AA 6061-T6, J. Strain Anal. Eng. Des., 53(7) (2018) 494-503.
- [5] P. Cavaliere, E. Cerri, A. Squillace, Mechanical response of 2024-7075 aluminium alloys joined by Friction Stir Welding, J. Mater. Sci., 40(14) (2005) 3669-3676.
- [6] M. Aonuma, K. Nakata, Dissimilar metal joining of 2024 and 7075 aluminium alloys to titanium alloys by friction stir welding, Mater. Trans., 52(5) (2011) 948-952.
- [7] M.B. Prime, T. Gn<sup>5</sup>aupel-Herold, J.A. Baumann, R.J. Lederich, D.M. Bowden, R.J. Sebring, Residual stress measurements in a thick, dissimilar aluminum alloy friction stir weld, Acta Mater., 54(15) (2006) 4013-4021.

- [8] I. Alinaghian, M. Honarpisheh, S. Amini, The influence of bending mode ultrasonic-assisted friction stir welding of Al-6061-T6 alloy on residual stress, welding force and macrostructure, J. Adv. Manuf. Technol., 95 (2018) 2757-2766.
- [9] A.R. Eivani, H. Vafaeenezhad, H.R. Jafarian, J. Zhou, A novel approach to determine residual stress field during FSW of AZ91 Mg alloy using combined smoothed particle hydrodynamics/neuro-fuzzy computations and ultrasonic testing, J. Magnes. Alloy, 9(4) (2021) 1304-1328.
- [10] E. Salvati, J. Everaerts, K. Kageyama, A.M. Korsunsky, Transverse fatigue behaviour and residual stress analyses of double sided FSW aluminium alloy joints, Fatigue & Fract. Eng. Mater. & Struct., 42(9) (2019) 1980-1990.
- [11] S. Delijaicov, M. Rodrigues, A. Farias, M.D. Neves, R. Bortolussi, M. Miyazaki, F. Brandão, Microhardness and residual stress of dissimilar and thick aluminum plates AA7181-T7651 and AA7475-T7351 using bobbin, top, bottom, and double-sided FSW methods, J. Adv. Manuf. Technol., 108 (2020) 277-287.
- [12] K. N. Salloomi, S. Al-Sumaidae, Coupled Eulerian-Lagrangian prediction of thermal and residual stress environments in dissimilar friction stir welding of aluminum alloys, J. Adv. Join. Process., 3 (2021) 100052.
- [13] M. Kaid, M. Zemri, A. Brahami, S. Zahaf, Effect of friction stir welding (FSW) parameters on the peak temperature and the residual stresses of aluminum alloy 6061-T6: numerical modelisation, J. Interact. Des. Manuf., 13 (2019) 797-807.
- [14] Y. Zhan, Y. Li, E. Zhang, Y. Ge, C. Liu, Laser ultrasonic technology for residual stress measurement of 7075 aluminum alloy friction stir welding, Appl. Acoust., 145 (2019) 52-59.

- [15] X. Liu, P. Xie, R. Wimpory, W. Li, R. Lai, M. Li, D. Chen, Y. Liu, H. Zhao, Residual stress, microstructure and mechanical properties in thick 6005A-T6 aluminium alloy friction stir welds, Metals, 9(7) (2019) 803.
- [16] K. Abdullah, P.M. Wild, J.J. Jeswiet, A. Ghasempoor, Tensile testing for weld deformation properties in similar gage tailor welded blanks using the rule of mixtures, J. Mater. Process. Technol., 112(1) (2001) 91-97.
- [17] M.B. Prime, The contour method: simple 2-D mapping of residual stresses. ASME International Mechanical Engineering Congress and Exposition, Vol. American Society of Mechanical Engineers, 19050 (2000) 121-127.
- [18] G.V.B. Lemos, R.M. Nunes, P. Doll, L. Bergmann, T.R. Strohaecker, J.F.D. Santos, Avaliação das tensões residuais em juntas soldadas de inconel 625 obtidas através da soldagem por fricção e Mistura mecânica, Soldagem & Inspeção, 22 (2017) 35-45.
- [19] P. Staron, M. Kocak, S. Williams, A. Wescott, Residual stress in friction stir-welded Al sheets. Physica B Condens, Matter, 350(1-3) (2004) E491-E493.
- [20] L.N. Brewer, M.S. Bennett, B.W. Baker, E.A. Payzant, L.M. Sochalski-Kolbus, Characterization of residual stress as a function of friction stir welding parameters in oxide dispersion strengthened (ODS) steel MA956, Mater. Sci. Eng. A, 647 (2015) 313-321.
- [21] G.V.B. Lemos, A.B. Farina, R.M. Nunes, P.H.C.P. da Cunha, L. Bergmann, J.F. dos Santos, A. Reguly, Residual stress characterization in friction stir welds of alloy 625, J. Mater. Res. Technol., 8(3) (2019) 2528-2537.



#### Journal of Stress Analysis

Vol. 8, No. 1 (2023) 27-33



ORIGINAL RESEARCH PAPER

## Investigation of Effect of Hyaluronic Acid Containing Medicine on Frictional Behavior of Synovial Fluid

Behnam Dehghani, Amir Torabi\*

Mechanical Engineering Department, Engineering Faculty of Shahrekord University, Shahrekord, Iran.

#### Article info

Article history: Received 14 January 2023 Received in revised form 29 July 2023 Accepted 27 August 2023

Keywords:
Elastohydrodynamic
Lubrication
Friction
Synovial fluid
Hyaluronic Acid

#### Abstract

Cartilage and synovial fluid ensure the smooth movement of natural joints to work with very little friction. However, the number of patients with joint diseases, which are usually related to cartilage destruction, constantly increases. Therefore, understanding the tribological behavior of synovial fluid is of great concern in order to reduce its degradation and maintain a reliable joint function. The purpose of this research is to provide insight into the frictional behavior of synovial fluid, focusing on its composition and especially hyaluronic acid (HA) content, velocity, and applied load on the joint. For this purpose, a pin-on-disc simulator was used. The tests were accomplished at three different movement velocities and under three loads of 30, 60, and 100N. During the tests, the lubricants were pure synovial fluid and synovial fluid with 10% and 20% of a traditional osteoporosis medicine, i.e. Cynogel. The test results showed that the friction strongly depends on the HA content of the lubricant. Studying the applied load effect on the friction coefficient, it was found that hyaluronic acid's rheological behavior could neutralize the medicine's effect under a light load at a slow speed. After adding Cynogel into the synovial fluid, the friction coefficient decreased under higher loads. The greatest changes were observed for the 20% combination, which led to about 20% and 30% improvement in the friction coefficient at high and medium velocities, respectively.

#### 1. Introduction

Due to joints, the movements of human body parts are very flexible and they have smooth movements. The joint mechanisms are naturally optimized with a minimal friction and protected against wear under different loads and velocity conditions. High wear resistance besides a slight friction is mainly exerted as a result of articular cartilage and its microstructural configuration. The tribology of joints is related to many key factors; therefore, synovial lubrication has greatly interested researchers [1, 2]. To obtain realistic performance of artificial synovial joints, researchers are try-

ing to analyze the lubrication mechanism and frictional characteristics of real joints to modify and implement prosthetic components [3]. The results of the research can be useful for increasing knowledge in the treatment of osteoarthritis, synovial joint replantation, artificial cartilage construction, and synovial diseases.

During the last two decades, a significant number of experiments and hypothetical studies have been reported about lubrication in synovial joints. The results showed that synovial lubrication is a mixed lubrication consisting of synovial fluid film lubrication, synovial fluid macromolecule boundary lubrication, and squeeze

\*Corresponding author: A. Torabi (Assistant Professor)

E-mail address: torabi@sku.ac.ir doi 10.22084/JRSTAN.2024.27951.1245

ISSN: 2588-2597



film lubrication under pressure by cartilage interstitial fluid [4, 5].

Synovial fluid consists of phospholipids, hyaluronic acid (HA), and lubricin. These molecules are ubiquitous in synovial fluid. All three molecules act synergistically and each has a different function to provide superior lubrication on the cartilage surface under high physiological pressures [6]. Apart from the timedependent friction regulation, macromolecules formed in the synovial fluid, such as proteoglycan lubricin, polysaccharide hyaluronic acid, and phospholipids, form the biological boundary lubrication on the cartilage surface. These macromolecular boundary lubricants facilitate low friction and wear resistance when two opposing cartilage surfaces come into contact. In healthy joints, the solid-solid cartilage contact does not occur. It can be concluded that the extremely low friction and excellent wear resistance of the joint are manipulated by the intervention of the mechanisms of squeeze film and boundary lubrication [7].

HA is a naturally existing substance in synovial fluid. When the joint has arthritis, the HA concentration in the synovial fluid decreases. If the synthetic form of HA is injected into the joint, its viscosity increases, and in this way, the movement of the joint becomes smoother and the pain is reduced. There is insufficient evidence to conclude the usefulness of HA, and it is impossible to comment with certainty on the benefits or harms of this injection [8].

Furmann et al. [9] investigated the synovial fluid composition, velocity, and load effect on the frictional behavior of synovial fluid. Their results showed that protein-based solutions, regardless of the concentration of the components, show almost a similar coefficient of friction. However, the behavior changes significantly with the addition of HA and phospholipids. Berli et al. [10] investigated the knee prosthesis lubrication model. with non-Newtonian fluid and porous rough materials. Their results showed that a larger deformation capacity promotes thick fluid layers despite the surface roughness. Forster et al. [11] studied the effect of loading time on the synovial fluid friction. In a lubrication condition, instead of a complete fluid film, the two-phase cartilage fluid bears a significant amount of load, and the boundary lubrication is governed. Farnham et al. [12] studied the effects of lubricants on the sliding biomechanics of synovial fluid under a physiological load. Their results showed that synovial fluid and HA solutions with a maximum viscosity of saline lubricants were at physiological shear rates of  $3^{-10}$ , and significantly increased lubricant recovery rates during sliding and reduced its amount to a minimum.

Murakami et al. [13] considered the synovial composition's effect on the articular cartilage's tribological behavior. They assessed the frictional changes of healthy and damaged articular cartilage samples against a glass plate lubricated with lubricants containing phospholipid, protein, and HA with a recipro-

cating wear test apparatus. They also concluded that good tribological condition in healthy synovial joints is due to effective lubrication mechanisms based on the proper combination of articular cartilage and synovial fluid. In another research, Murakami et al. [14] investigated the lubrication of an articular cartilage and an artificial hydrogel cartilage. They found that the superior lubrication performance of healthy natural synovial joints is realized not by a single lubrication mode, but by a synergistic combination of multi-mode mechanisms such as fluid film, two-phase, hydration, gel film, and boundary lubrication. Burris et al. [15] demonstrated the role of slippage and hydrodynamics in joint lubrication. Their results declared that the effect of tribological hydration was more prominent in increasing the velocity, under reduced loads, in the presence of hyaluronic acid, and with increasing the size of the convergence zone. This trend is consistent with the hypothesis that tribological hydration is induced by external hydrodynamic pressure.

Hilser et al. [16] confirmed the synergistic effect of phospholipids and HA in reducing cartilage friction, and they also hypothesized that this effect is because of hydration lubrication. Mederake et al. [17] investigated the effect of three synovial lubricants (sodium chloride, fetal calf serum, and HA) on friction in nine complete carpometacarpal joints of a sheep. Friction in injured joints is significantly increased compared to healthy joints. Comparing different lubricants, the results show the greatest reduction in friction for HA. Rabenda et al. [18] showed a strong relationship between the molecular weight of HA and the rheological properties of its solutions, and they could not find a clear relationship between the molecular weight of HA and the coefficient of friction. Bell et al. [19] showed that HA is an effective boundary lubricant under static conditions and is less effective in dynamic conditions. Some studies recently intend to supplement injection to the joint, and the effect of friction reduction of these medications is investigated [20–22]. The effectiveness of these drugs has not been determined. Some evaluate them as useful and some as ineffective.

Various studies are focused on joint, cartilage, and synovial fluid behavior. However, frictional modeling and evaluation of synovial medication have not been fully understood. Therefore, the present study is designed to provide a specific analysis of the frictional behavior of synovial fluid considering the effect of the combination of synovial fluid and Cynogel (a drug containing the HA compound), entraining velocity, and load. The test conditions were designed based on previous studies to mimic typical daily activities (slow, normal walking, stair climbing - high load). Furthermore, since the synovial fluid composition is supposed to play a key role in synovial lubrication, the focus is on the concentration and mutual interactions of synovial fluid and HA.

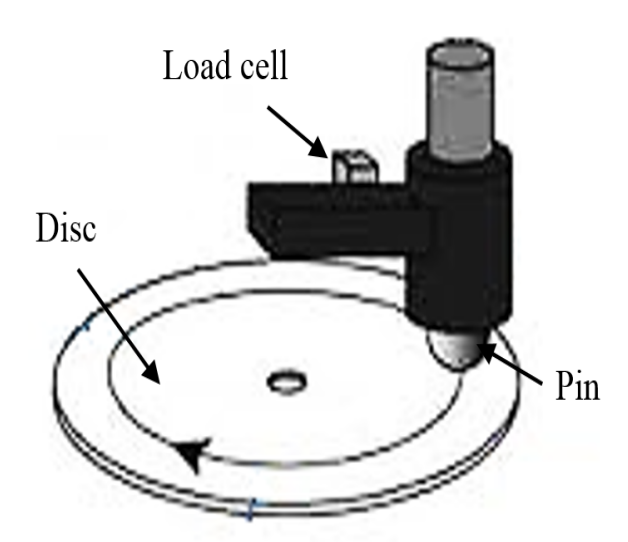




Fig. 1. A view of the pin-on-disc tribometer and the schematic of its operation.

#### 2. Materials and Methods

The pin-on-disc tribometer device shown in Fig. 1 is usually used for investigation of the effect of lubricants on the friction coefficient and the amount of wear under a specific load and velocity according the ASTM G-99 standards. As seen in Fig. 1, in this device, the lubricant is presented between two pieces of disc and pin. The disc rotates at a constant speed, and the pin is loaded on the disc with a certain load. With the help of the load cell device, the friction force between the pin and the disc is measured. The load cell of the device was calibrated with the help of a special weight and the method provided by the device manufacturer. Usually, the pin is made of hard material and the disc is made of softer material, and their surface is polished to the desired roughness. In this study, the 6-mm thick discs were made of St37 steel with a diameter of 90mm, and the pin was made of 52100 steel with a hardness of 64 Rockwell. The discs were polished to a roughness of  $< 1\mu m$  to ignore the effect of surface roughness on the friction results.

The pin can be placed at three different radial distances of 27, 48, and 66mm from the center of the discs; thus, at a fixed rotational velocity of the device, i.e. 44rpm, three different linear velocities of 0.124, 0.223, and 0.3m/s can be achieved. Fig. 2 shows the disc sample after the test and the path of the pin movement on the disc in this study.

As mentioned earlier, the lubricant used in these tests was prepared from the tapped synovial fluid of patients suffering from osteoarthritis, who were mostly over 60 years old and had been referred to a specialist doctor for aspiration of the knee joint synovial fluid. Cynogel medication (sodium hyaluronate 1.6% with a high molecular weight) was also used to investigate the effect of HA compounds. This drug is available in the

form of a ready-made syringe with a concentration of 32mg in a volume of 3ml in the pharmaceutical market. In this research, synovial fluid alone and synovial fluid with the addition of different amounts of 10% and 20% by the volume of Cynogel were used as a lubricant in the tests. Therefore, three different loads, three velocities, and three different lubricant combinations were tested, i.e. a total of 27 tests. To check repeatability and eliminate errors as much as possible, each test was repeated three times. Therefore, in this research, 27 fully polished double-sided discs with the dimensions mentioned above and 27 pins were prepared using ready-made roller bearings. Each disc provides the possibility of 6 tests. The various parameters of the tests performed in this research are given in Table 1.

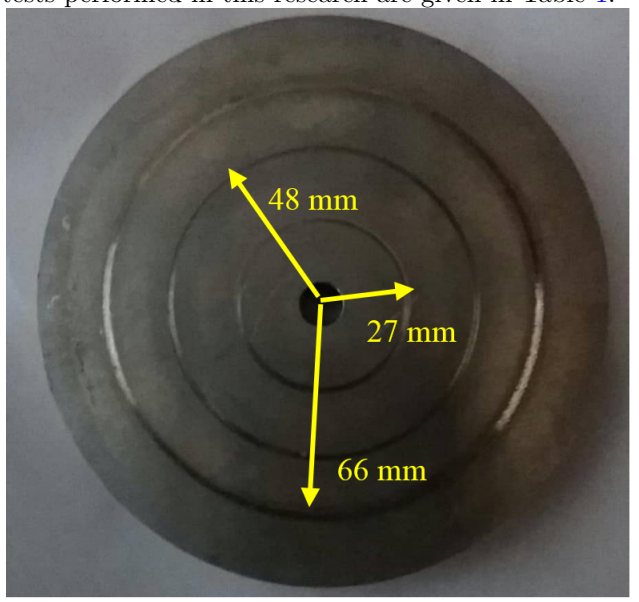


**Fig. 2.** Disc sample after the test and the positions of pin trajectory.

Table 1
Load, velocity, and lubricant parameters of the designed tests.

Test No.	Load (N)	Medicine (%)	Disc velocity (m/s)
1	30	0	0.124
2	30	10	0.124
3	30	20	0.124
4	30	0	0.223
5	30	10	0.223
6	30	20	0.223
7	30	0	0.300
8	30	10	0.300
9	30	20	0.300
10	30	0	0.124
11	60	10	0.124
12	60	20	0.124
13	60	0	0.223
14	60	10	0.223
15	60	20	0.223
16	60	0	0.300
17	60	10	0.300
18	60	20	0.300
19	100	0	0.124
20	100	10	0.124
21	100	20	0.124
22	100	0	0.223
23	100	10	0.223
24	100	20	0.223
25	100	0	0.300
26	100	10	0.300
27	100	20	0.300

At first, when the pin contacts the polished surface, their roughness interacts with each other, and sometimes they are welded together. After beginning the sliding of the surfaces, the welded roughness pushes and pulls each other which may cause them to break or deform. The change of the roughness, at the beginning of the movement, is called the running-in process. In order to consider running-in, the friction force was measured after a relatively long distance of 200m when the roughness of the surfaces was more smoothened. Therefore, in this way, the possible effect of initial roughness deformation or probable wear was prevented.

#### 3. Results

The pin-on-disc test device measures the friction force during the test time. According to the rotational velocity of the disc and the radius of the pin on it, the distance traveled during the test can be obtained. A sample of the reported data of the friction coefficient by the device for a normal load of 30N at three different velocities is shown in Fig. 3. Also, this figure presents the data for three different combinations of synovial fluid and hyaluronic-containing medicine. The static friction is larger than the dynamic friction. This depends on

the nature of the materials in contact: it is a result of some highly complicated phenomena at a microscopic level such as asperity interaction. After the motion, the running-in wear process causes the surface asperity amplitude to decrease. This gradually reduces friction to an asymptomatic value. In lubrication, increasing the velocity forms a thicker fluid layer. As expected, it can be seen in the results that with the increase in velocity, a thicker layer forms, and the possibility of the surface roughness interaction as well as the friction coefficient is significantly reduced. For example, in the case of synovial fluid lubrication, only increasing the velocity from 0.124m/s to 0.223m/s reduced the friction coefficient by 12%. A further increase in the velocity up to 0.3m/s brings this reduction to 55%.

The purpose of this study is to investigate the effect of drugs containing HA. Besides synovial fluid, the combination of 10% and 20% of a famous traditional medicine in the Iranian market (Cynogel) with synovial fluid at different velocities for a specified load of 30N is presented in Fig. 3B and 3C. The reduction in friction with increasing the surface velocity is similar to synovial fluid. In the 10% compound, the friction coefficient decreases by 13.8% when the velocity increases from 0.124 to 0.223m/s, and it decreases to 59.4% for the surface velocity of 0.3m/s. In the 20% compound, these reductions are 7% for the surface velocity of 0.223m/s and 53% for 0.3m/s. Therefore, adding HA to synovial fluid under this specific load does not make a significant difference in the reduced friction caused by the increased velocity.

Adding HA under 30N load, for all three mentioned velocities does not affect the friction coefficient significantly. For example, for the synovial fluid lubricant, the average friction coefficient at 0.124m/s is 8% lower than synovial fluid and 10%HA, and 11% higher than synovial fluid and 20%HA. At the velocity of 0.224m/s, these values are 7% lower and 5.8% higher, respectively. At the velocity of 0.3m/s, the friction coefficient for the synovial fluid lubricant is 2% and 8% higher than 10% and 20% HA, respectively. Under this relatively low load, for low and medium velocities, adding the medicine slightly not only reduces the friction coefficient, but somehow increases its value. While the addition of more HA is more efficient.

Fig. 4 shows the changes in friction coefficient for all experiments. Different loads and different velocities and the combination of different lubricants affect the coefficient of friction. Formerly, the changes of friction were described for the light load. However, under higher loads, the trend of change in friction coefficient is similar to each other, i.e. increasing the velocity reduces the friction coefficient. Under a moderate load, the coefficient of friction decreases intensively with increased velocity. Under high loads, the decrease in friction coefficient with the increased velocity has a constant proportionality.

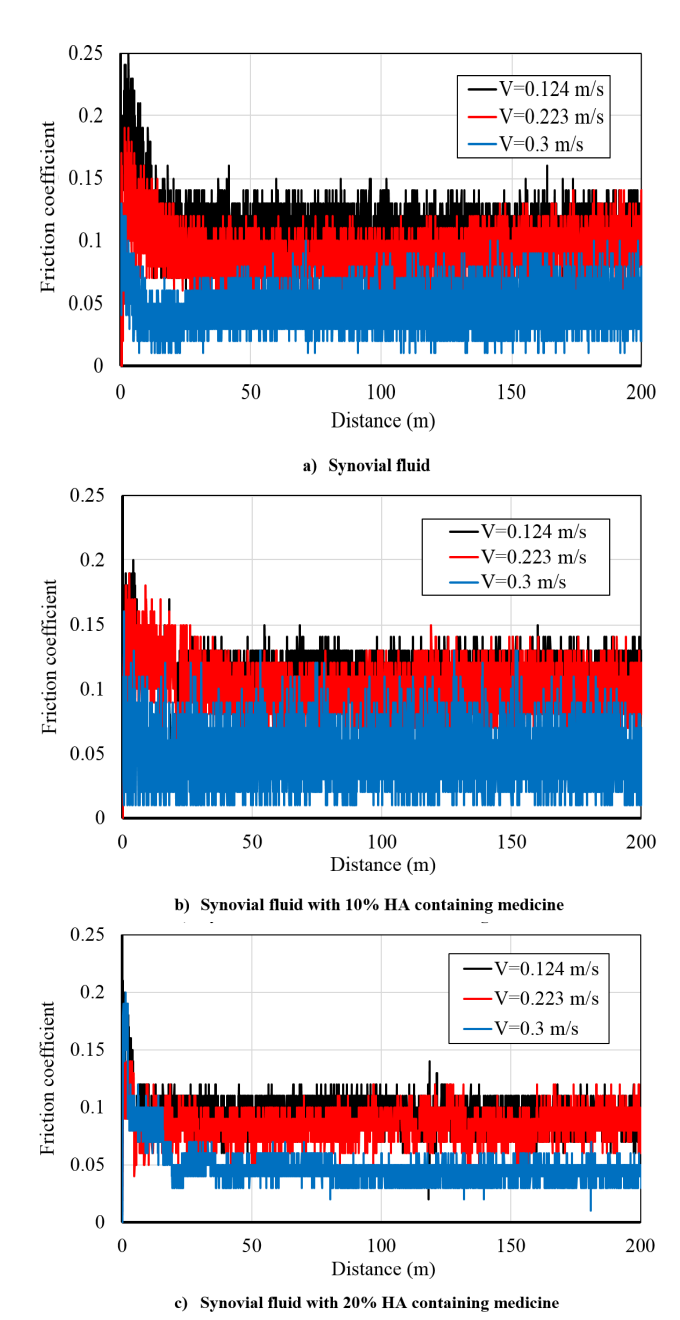


**Fig. 3.** Changes in friction coefficient for a load of 30N at different velocities for synovial fluid and its combination with a drug-containing HA.

Investigating the effect of lubricant combination or the percentile of medicine used on the friction coefficient under 60 and 100N load shows that even the low-drug content, i.e. 10%, results in a significant decrease in the friction coefficient. This reduction in friction can be seen at different velocities. The reduction rate of the coefficient of friction in the composition of 20% is higher. At 60Nm, adding 10% of the drug-containing HA will decrease the friction coefficient by about 12%, and at 100Nm, about 20% to 35% decrease in friction coefficients can be seen at different speeds. By adding 20% of the drug-containing HA at 60Nm, the friction coefficient decreases by between 25% and 30%, and at

 $100\mathrm{Nm},$  this decrease will be between 20% and 30% at different velocities.

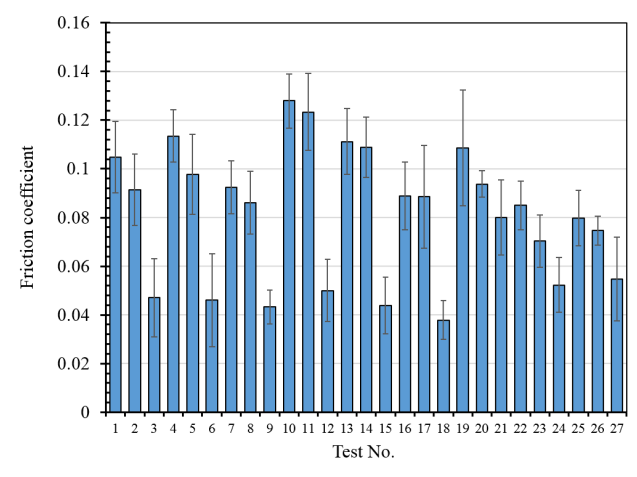


Fig. 4. Friction coefficient variation for various tests.

Synovial fluid is the ultrafiltration of blood plasma (that is, plasma free of large proteins) enriched with locally synthesized polysaccharide molecules called hyaluronan. The hyaluronan molecule in synovial fluid is composed of a very long unbranched, strongly anionic polymer of 25,000 repeating disaccharide units. During loading, which is relatively fast, the hyaluronan chains are randomly connected to each other in the solution; therefore, the response of synovial fluid is quasi-elastic; as a result, the joint can withstand severe loading. On the other hand, under slow and long flow conditions, the chains are forced to align and, consequently, the bonds between them are replaced by water molecules. This results in a partial separation of the hyaluronan chains, leading to their ability to slide past each other more freely, and synovial fluid responds like a shear-thinning viscous fluid. A sharper decrease in the friction coefficient at higher velocities indicates this thin shear property. At small shear rates, the fluid's resistance to movement is high, but with the increase in the shear rate, the fluid becomes more fluent. Therefore, the addition of the material with shear-thinning property can be beneficial against the rapid and large loads that occur during walking and joint activity.

On the other hand, osteoarthritis is a common joint disease characterized by the destruction of articular cartilage and includes changes in the structure and composition of cartilage [4]. The damaged cartilage surface leads to increased friction and causes a slight disruption of the two-phase lubrication mechanism in articular cartilage. HA is a suggested shear-thinning material that shows a beneficial effect on the friction reduction and is very compatible with synovial fluid.

#### 4. Conclusions

Here a challenging problem of using the osteoporosis treatment medicine is considered experimentally using the pin-on-disc simulator. Different compositions of medicine (10% and 20%) and synovial fluid are used as a lubricant. Since all these people had the same disease and were in close age groups, we can more confidently consider the effect of the drug for reduction in the joint friction. The effect of load and velocity is also investigated. The following results are concluded:

- The friction coefficient is reduced with increasing velocity for all types of the lubricant due to improving the lubrication mechanism.
- However, for light load and low velocity, this expectation is not met, and some increase in the friction coefficient is seen with increasing velocity. This is due to the increased viscous friction of the lubricant.
- As the velocity increases, the effect of the viscous friction decreases and the coefficient of friction reduces.
- A higher concentration of HA shows better a tribological condition.
- When 20% of the medicine is compounded with synovial fluid, the friction coefficient reduces drastically with 0 and 10% combination. This demonstrates the importance of using a sufficient dosage of the medicine to have an acceptable response.
- The study limitation is the use of a metallic material for the surfaces while the perfect test should be performed with the same surface materials, i.e., natural joint cartilage. This is due to the fact that it was difficult to make the pin and disk from cartilage, and also the elastic pin caused very high fluctuations in data. However, the results are comparative so they can be generalized to the real situation.

#### References

- de Vries, E.G., van Minnen, B.S., Wu, Y., Matthews, D.T. and van der Heide, E., 2023. Tribological behaviour of a synthetic synovial fluid and polyurethane in biomedical implants. Biotribology, 33, p.100242.
- [2] Gangi, L.R., Pagon, A.D., Pellicore, M.J., Kroupa, K.R., Murphy, L.A., Ateshian, G.A. and Hung, C.T., 2024. Synovium friction properties are influenced by proteoglycan content. J. Biomech., p.112272.
- [3] Jiajia, C.E.N., ZHANG, D., Qin, C.H.E.N., ZHANG, X., Cunao, F.E.N.G., Haiyan, F.E.N.G.

- and Kai, C.H.E.N., 2024. The influence of synovial fluid components on the tribological behavior of "soft-soft" joint pair materials. Journal of Tsinghua University (Science and Technology), 64(3), pp.454-470.
- [4] Lin, W. and Klein, J., 2021. Recent progress in cartilage lubrication. J. Adv. Mater., 33(18), p.2005513.
- [5] Ruggiero, A., 2020. Milestones in natural lubrication of synovial joints. Front. Mech. Eng., 6, p.52.
- [6] Ateshian G.A., 2009, "The Role of Interstitial Fluid Pressurization in Articular Cartilage Lubrication", J. Biomech., 42(9), 1163-1176.
- [7] Charnley J., 1960, "The lubrication of animal joints in relation to surgical reconstruction by arthroplasty", Ann Rheum Dis., 19, 10-19.
- [8] Park J.Y., Duong C.T., Sharma A.R., Son K.M., Thompson M.S., Park S., et al., 2014, "Effects of Hyaluronic Acid and γ-Globulin Concentrations on the Frictional Response of Human Osteoarthritic Articular Cartilage. PLoS One, 10(2): e0118040.
- [9] Furmann D., Nečas D., Rebenda D., Čípek P., Vrbka M., Křupka I., Hartl M., 2020, "The Effect of Synovial Fluid Composition, Speed and Load on Frictional Behaviour of Articular Cartilage", Materials, 13, 1334-1350.
- [10] Berli M., Campana D., Ubal S. and Di Paolo J., 2009, "Lubrication Model of A Knee Prosthesis, With Non Newtonian fluid and Porous Rough Material", Lat. Am. Appl. Res., 39(2), 105-111.
- [11] Forster H. and Fisher J., 1996, "The influence of loading time and lubricant on the Friction of articular cartilage", Proc. Inst. Mech. Eng., 210(2):109-119.
- [12] Farnham M. S., Larson R. E., Burris D. L., and Price C., 2020, "Effects of Mechanical Injury on the Tribological Rehydration and Lubrication of Articular Cartilage", J. Mech. Behav. Biomed. Mater., 101, 103422.
- [13] Murakami T., Yarimitsu S., Nakashima K., Sawae Y., and Sakai N., 2013, "Influence of synovia constituents on tribological behaviors of articular cartilage", Friction, 1, 150–162.
- [14] Murakami T., Yarimitsu S., Nakashima K., Yamaguchi T., Sawae Y., Sakai N., and Suzuki A., 2014, "Superior lubricity in articular cartilage and artificial hydrogel cartilage", Proc. Inst. Mech. Eng., Part J, 228(10), 1099-1111.

- [15] Burris D.L., Ramsey L., Graham B.T., Price C., and Moore A. C., 2019, "How Sliding and Hydrodynamics Contribute to Articular Cartilage Fluid and Lubrication Recovery", Tribol. Lett., 67, 46.
- [16] Hilšer P., Suchánková A., Mendová K., Eleršič Filipič K., Daniel M., Vrbka M., 2021, "A new insight into more effective viscosupplementation based on the synergy of hyaluronic acid and phospholipids for cartilage friction reduction", Biotribology, 25, 100166.
- [17] Mederake M., Trappe D., Jacob C. et al., 2022, "Influence of hyaluronic acid on intra-articular friction – a biomechanical study in whole animal joints", BMC Musculoskelet. Disord., 23, 927.
- [18] Rebenda D., Vrbka M., Čípek P., Toropitsyn E., Nečas D., Pravda M., and Hartl M., 2020, "On the Dependence of Rheology of Hyaluronic Acid Solutions and Frictional Behavior of Articular Cartilage", Materials, 13(11): 2659.
- [19] Bell C.J., Ingham E., Fisher J., 2006, "Influence of

- hyaluronic acid on the time-dependent friction response of articular cartilage under different conditions", Proceedings of the Institution of Mechanical Engineers, Proc. Inst. Mech. Eng H., 220(1), 23-31.
- [20] de Roy, L., Eichhorn, K., Faschingbauer, M., Schlickenrieder, K., Ignatius, A. and Seitz, A.M., 2023. Impact of hyaluronic acid injection on the knee joint friction. Knee Surg. Sports Traumatol. Arthrosc., Arthroscopy, 31(12), pp.5554-5564.
- [21] Su, C.Y., Lu, Y.F., Lu, Y.C., Huang, C.H. and Fang, H.W., 2023. Potential lubricating mechanism of hyaluronic acid for a reduction of albumin-mediated friction in the artificial joint system. Lubricants, 11(5), p.210.
- [22] Impergre, A., De Vecchi, F., Schmid, T.M. and Wimmer, M.A., 2024. Tribological assessment of novel lipid-based intra-articular injectable and hyaluronic acid as joint fluid supplements. Osteoarthr. Cartil., 32(6), pp.783-784.



#### Journal of Stress Analysis

Vol. 8, No. 1, 2023-24, 35-55



ORIGINAL RESEARCH PAPER

## NSSFEM: Nonlinear Spectral Stochastic Finite Element Method for Analysis of Structures with Elastoplastic Material

Hosseinali Rahimibondarabadi<sup>\*</sup>, Seyed Sajad Mousaviamjad

Department of Civil Engineering, Yazd University, Yazd, Iran.

#### Article info

Article history:
Received 10 April 2023
Received in revised form
24 August 2023
Accepted 17 September 2023

Keywords:

Karhunen-Loève expansion Polynomial chaos Elastoplastic materials Spectral stochastic finite element method

#### Abstract

The stochastic finite element method is one of the most effective tools for analyzing systems with uncertainty in computational stochastic mechanics. In this research, a novel approach called the nonlinear spectral stochastic finite element method (NSSFEM) was developed to analyze structures with nonlinear materials. The proposed NSSFEM incorporates uncertainty in both loads and elastic modulus. In the first step, the input random variables are modeled using the operators of NSSFEM, and an appropriate number of terms from the Karhunen-Loève expansion is selected. Next, the stiffness matrix is formed, assuming linear material behavior as the problem-solving begins. Subsequently, the responses are modeled as random processes and expanded using polynomial chaos. During each increment of the solution process, the stress state at the Gaussian points is checked before completing a sub-increment. If the material yielding criteria are activated, the stresses are modified according to plasticity conditions, thereby correcting the solutions. This iterative process continues until the problem is fully resolved and the desired solution is achieved. The displacements obtained through the proposed NSSFEM demonstrate an impressive accuracy of 97% when compared with results from the Monte Carlo method. The source code of the proposed NSSFEM is available at https://github.com/seyedsajadmousavi/NSSFEM

#### Nomenclature

Ω	Sample space	$\sigma$	Algebra in subsets $\Omega$
P	Probability measurements	X	A random variable
$f_x(x)$	Probability density function (PDF)	$\mu_{f(x)}$	Mean of the random field
$\sigma_{f(x)}$	Standard deviation	$\lambda_n$	Eigenvalues
$\phi_n(x)$	Eigenfunctions	$C(x_1,x_2)$	Covariance
$k_0^{(e)}$	mean stiffness	$C^{ep}(x,\theta)$	The elastoplastic hardness matrix
$V^{(e)}$	Volume of the element	E	Modulus of elasticity of the materials
$d\sigma(x,\theta)$	Stress increment	$d\epsilon^e(x,\theta)$	Strain increment
$\Delta k^{(e)}$	Stochastic parts of the stochastic stiff-		
	ness matrix		

<sup>\*</sup>Corresponding author: H. Rahimibondarabadi (Associate Professor)

E-mail address: h\_rahimi@yazd.ac.ir doi 10.22084/JRSTAN.2024.29190.1255

ISSN: 2588-2597



#### 1. Introduction

#### 1.1. Stochastic Approach in Analysis of Structures

Considering the realization of the scientific community on the importance of the stochastic approach in engineering problems and the significant effect of uncertainties on the behavior of systems, powerful computational methods have been developed. These approaches allow the analysis and design of a variety of engineering systems on a large scale with the help of powerful computing tools considering complex conditions including the application of uncertainty. In structural engineering, uncertainties can include structural inputs such as material properties, geometry, boundary conditions, or loading [1–6]. As the case may be, these properties are described by statistical concepts such as random variables, random processes, or random fields. One of the most useful tools for analyzing systems with uncertainties in computational stochastic mechanics is the stochastic finite element method (SFEM), which is based on the increment of the classical finite element method (FEM). From a mathematical point of view, SFEM can be considered a computational method for solving stochastic partial differential equations [7–12].

#### 1.2. Related Works

In several studies, the problems of convergence and error estimation of this method have been studied in detail. In fact, these two aspects of SFEM are complementary and interdependent. A fundamental problem in stochastic finite element modeling is the uncertainty of system input parameters. The key point of a problem-solving method is the stochastic finite element matrix formulation, which is divided into four general categories based on the calculated technique for modeling uncertainty: Monte Carlo simulation (MCS), perturbation method, spectral decomposition method, and weighted integral method. To obtain system responses, several different SFEMs have been proposed, including the Newman expansion, the Taylorturbulence series expansion method, the stochastic response validation method, the Monte Carlo simulation, and the spectral stochastic finite element method (SSFEM) [13–16]. Due to its capacity to represent a broad range of complicated situations, the Monte Carlo simulation technique is a commonly used simulation approach [13]. The fundamental concept is to construct samples based on the statistical features of random variables, then solve differential equations with stochastic partial derivatives using the finite element technique to obtain a wide variety of solutions. Although relatively accurate results can be obtained by considering the appropriate number of samples, this method is computationally expensive in the problems with a large number of uncertain parameters as well

as large systems. On the other hand, in systems in which the materials used have nonlinear behavior, it is possible to achieve the solution by incremental methods, which itself requires a lot of computational costs. Therefore, in these cases, finding methods that reduce the computational volume will be inevitable [13]. Huo et al. introduced a novel non-intrusive SFEM (NIS-FEM) for usefully calculating stochastic responses and reliabilities of structures. In the first step, the direct probability integral approach (DPIM) was extended to get the PDF of stochastic response by solution of probability density integral equation (PDIE). Then, the NISFEM using DPIM decoupled the classical FEM and PDIE to compute the stochastic output and reliabilities of uncertain plates, and the discretization and quantification of random fields of Young's modulus and thickness were applied via Karhunen-Loève expansion (KLE). The performance of the NISFEM compared with Monte Carlo simulation (MCS) shows that Huo et al. achieved the better accuracy [17]. Andres and Hori proposed a novel method for non-linear elastoplastic bodies based on SFEM, as a generalization of the SFEM for linear elastic materials. The principle characteristic feature of this method was the proposal of two fictitious structures whose behaviors gave maximum and minimum bounds for the mean of variables. The bounding structures are thoroughly derived from a given material feature. The performance of methods is evaluated by MCS. It is illustrated that this method can estimate means and standard divisions of field variables even when the structure has a larger standard division of the body features [18]. Stavroulakis et al. reported the benefits of the graphical processing unit (GPU) for addressing intrusive stochastic mechanics problems. The computational performance of using GPU for solving the problems illustrated an improvement of SSFEM [19].

Sepahvand and Marburg proposed a non-samplingbased SFEM for vibroacoustic analysis of fiberreinforced composite plates with uncertain Young's modulus and damping ratio. The performance evaluation shows numerous effects of uncertainties in diverse frequency ranges. The computed random transmission loss illustrates an acceptable error rate compared to the results obtained by MCS [20]. Appalanaidu et al. introduced a method based on the generalization of stochastic finite element for damage evaluation. The SSFEM is extended where the non-Gaussian random fields are defined by employing an optimal linear expansion scheme. MCS is used to evaluate the stress. The performance of this method is shown with a numerical example including a circular pipe [21]. Researchers have always sought appropriate solutions to this problem, one of which is SSFEM first proposed by Ghanem and Spanos [22]. In this method, KLE is used to discretize a random field that describes uncertain parameters. While the system's responses remain stochastic and are estimated by a chaotic polynomial [13, 20, 23–25]. Since SSFEM has good accuracy and efficiency, it is very popular among researchers and has been used in many studies. This research has been documented in a report. Some studies have used the aforementioned strategy to investigate the following topics: wave propagation analysis, vibration analysis of fiberreinforced composites [20], composite plates [26–28], random creep failure prediction [21], earth dams [29], shells [10, 30], wooden structures [31], elastodynamic issues in the time domain [7], and a variety of other instances have all been investigated. Lacour et al. looked into the nonlinear behavior of uncertain materials without taking into account the loading system's uncertainty, and their findings were provided [32]. However, certain loading was assumed in a wide range from studies presented for SSFEM, the research by Yazdani et al. can be mentioned among the limited researches in which loading is also assumed to be uncertain [13].

The following are the limitations of the state-of-theart:

- Computational complexity to calculate the structural responses
- Speed of accessing the structural responses
- Error rate of the structural responses

#### 1.3. The Proposed Method

In this study, the generalization of SSFEM is utilized to reduce the computational complexity associated with structural responses. The key contributions of this paper are summarized as follows:

- 1) Incorporating uncertainty in materials and loads
- 2) Modeling structures with nonlinear materials
- 3) Reducing computational complexity for calculating structural responses
- 4) Enhancing the speed of accessing structural responses
- 5) Decreasing the error rate of structural responses
- 6) Employing the proposed NSSFEM to analyze the reliability of structures

The remainder of this paper is organized as follows: Section 2 describes the materials and methods. Section 3 introduces the proposed NSSFEM. Results and discussions are presented in Section 4, followed by the conclusion in Section 5.

#### 2. Materials and Methods

The first step in analyzing uncertain systems is to provide system inputs. These inputs usually consist of mechanical and geometric properties as well as system

loading. Some parameters for which uncertainty can be considered include: Young's modulus, Poisson's ratio, yield stress, the cross-sectional geometry of physical systems, material and geometric defects of shells, loading, etc. In general, uncertainty in a complete probability space  $(\Omega, F, P)$  has been defined, including sample space  $\Omega$ , algebra  $\sigma$  in subsets  $\Omega$ , and probability measurements P. In modeling uncertainties in an engineering system, the terms random fields, random processes, and random variables are used when the uncertainties depend on the dimension of space, time, or are independent of both, respectively. An appropriate method to describe these values, which may have uncertainties in time or space is to implement random processes and fields whose probability distributions and correlation structures can be defined through experimental measurements. However, in many cases, there are assumptions about these probabilistic features due to the lack of relevant empirical data. The two main categories of random processes and fields can be defined based on their probability distributions: Gaussian and non-Gaussian. [13, 15, 16, 33–35].

#### 2.1. Random Variables

One way to show uncertainty is to consider the parameters as random variables. Where the variable X, whose value is independent of time and place, is a function for mapping the sample space  $\Omega$  in a range of real numbers  $R(X:\Omega\to R)$ . Fig. 1 schematically shows the performance of a random variable.

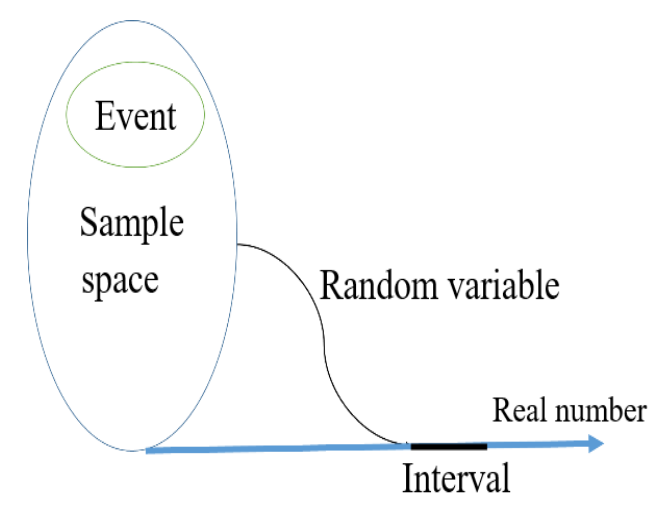


Fig. 1. Schematic performance of a random variable.

The probability of occurrence of a random variable X in the closed interval [a,b] can be calculated by Eq. (1):

$$P(a \le X \le b) = \int_a^b f_x(x) \, \mathrm{d}x \tag{1}$$

Where  $f_x(x)$  is a probability density function (PDF).

#### 2.2. Random Field

To address uncertainty in systems, the inputs must first be computed as a random field using a mathematical model capable of expressing a large number of phenomena oscillating in the form of a variable or continuous variables with an unexpected pattern of behavior. If the inputs are treated as a random field, a system of equations with stochastic partial derivatives will dominate, with uncertain and stochastic solutions. KLE and chaotic polynomial expansion (PCE) methods, which are described below, are used to model the random input parameters and system random solutions, respectively.

#### 2.3. Discretization of Random Gaussian Input Fields Using KLE

Despite the fact that most random values in engineering systems are non-Gaussian, the assumption of a possible Gaussian distribution is often used because of the simplicity and lack of relevant experimental data. A wide range of methods developed to simulate Gaussian random processes and fields were used in this study using the KLE method. KLE can be considered as a special case of orthogonal series expansion in which orthogonal functions are selected as special functions of the second type of Fredholm integral Eq. and auto covariance function as the kernel [2, 13, 20, 22, 36, 37]. Suppose that  $f(x, \theta)$  represents a random field in the DR domain with a function defined as  $(f: D \times \Omega \to R)$  in a perfect probability space  $(\Omega, \mathcal{F}, P)$  for  $x \in D$  and  $\theta \in \Omega$  where the mean values of  $f(x, \theta)$  are:

$$\mu_{f(x)} = \int_{a}^{b} f(x, \theta) \, \mathrm{d}\theta \tag{2}$$

And for the covariance function  $x_1, x_2 \in D$  we will have:

$$C(x_1, x_2) = \langle f(x_1, \theta) - \mu_f(x_1) \rangle \langle f(x_2, \theta) - \mu_f(x_2) \rangle \quad (3)$$

Now if  $\mu_{f(x)}$  and  $\sigma_{f(x)}$  represent the mean and standard deviation of the random field, respectively, the expansion of KLE will be:

$$f(x,\theta) = \mu_{f(x)} + \sigma_{f(x)} \sum_{n=1}^{N} \sqrt{\lambda_n} \phi_n(x) \xi_n(\theta)$$
 (4)

Where  $\mu_{f(x)}$  denotes the mean of the field,  $\lambda_n$  and  $\phi_n(x)$  represent the eigenvalues and eigenfunctions of covariance  $C(x_1, x_2)$ , respectively, n is a set of non-correlated variables, and N represents the number of KLE expansion terms. Also,  $\xi_n(\theta)$  is a set of non-correlated random variables with zero mean and unit variance. The eigenvalues and eigenvectors are obtained using the Fredholm quadratic integral equation

as follows:

$$\int_{D} C(x_1, x_2) \phi_n(x_1) \, \mathrm{d}_{x_1} = \lambda_n \phi_n(x_2) \tag{5}$$

#### 2.4. Representation of the Solutions By PCE

Random processes and fields are represented by polynomial chaos (PC), which are created by expanding a series of orthogonal polynomials via a sequence of random variables with definite coefficients [13, 15, 16, 23, 38]. Norbert Wiener presented the PC notion based on the homogeneous PC theory for Gaussian random variables as follows:

$$U(\theta) = a_0 \Gamma_0$$

$$+ \sum_{i_1=1}^{\infty} a_{i_1} \Gamma_1(\xi_{i_1}(\theta))$$

$$+ \sum_{i_1=1}^{\infty} \sum_{i_2=1}^{i_1} a_{i_1 i_2} \Gamma_2(\xi_{i_1}(\theta), \xi_{i_2}(\theta))$$

$$+ \sum_{i_1=1}^{\infty} \sum_{i_2=1}^{i_1} \sum_{i_3=1}^{i_2} a \Gamma_3(\xi_{i_1}(\theta), \xi_{i_2}(\theta), \xi_{i_3}(\theta))$$

$$+ \dots$$
(6)

Where,  $a_0, a_{i_1}, a_{i_1 i_2}, \ldots$  are the constant coefficients, and  $\Gamma_P$  is the p-th PC degree of the standard Gaussian random variable obtained as follows:

$$\Gamma_P(\xi) = (-1)^P \frac{\partial^P}{\partial \xi_{i_1} \dots \partial \xi_{i_P}} e^{-\frac{1}{2}\xi^T \xi}$$
 (7)

Now if we want to rewrite Eq. (6) as follows, there is:

$$U(\theta) = u_0 \psi_0(\xi(\theta)) + u_1 \psi_1(\xi(\theta)) + u_2 \psi_2(\xi(\theta)) + \dots$$

$$= \sum_{i=0}^{\infty} u_i \psi_i(\xi(\theta))$$
(8)

Where  $u_j$  and  $\psi_j$  correspond to  $a_0, a_{i_1}, a_{i_1 i_2}, \ldots$  and  $\Gamma_P$ , respectively. Given that the PCE is orthogonal, it meets the following conditions:

$$\psi_0(\theta) = 1, \langle \psi_j(\theta) \rangle = 0, \langle \psi_j(\theta) \psi_k(\theta) \rangle = \langle \psi_j^2(\theta) \rangle \delta_{jk}$$

where  $\delta_{jk}$  is the kronecker delta.

#### 3. Formulation of a SFEM

The expanded random field is used to formulate the stochastic matrix of each finite element (e). For a special case where the modulus of elasticity is defined as a random spatial variable in a homogeneous random field f(x, y, z), we will have an element to calculate

the stiffness of the element: [13–16]

$$\int_{V^{(e)}} B^{(e)T} D_0^{(e)} B^{(e)} dV^{(e)} + \int_{V^{(e)}} B^{(e)T} D_0^{(e)} B^{(e)} f^{(e)}(x, y, z) dV^{(e)}$$

$$k^{(e)} = k_0^{(e)} + \Delta k^{(e)}$$
(9)

Where  $k_0^{(e)}$  and  $\Delta k^{(e)}$  are the mean stiffness and stochastic parts of the stochastic stiffness matrix, respectively.  $B^{(e)}$  represents the strain-displacement matrix,  $D_0^{(e)}$  is the mean value of the stress-strain matrix, and  $V^{(e)}$  denotes the volume of the element. The general stochastic matrix is formed as follows:

$$K = \sum_{i=1}^{Ne} k^e = K_0 + \Delta K \tag{10}$$

Where Ne is the number of finite elements in the problem. Finally, the analysis of stochastic finite elements is obtained by algebraically solving the following equation:

$$P = (K_0 + \Delta K)u \tag{11}$$

Where P and u are node loading and displacement vectors, respectively. Assuming that the modulus of elasticity of the materials (E) used is a Gaussian spatial random variable with a mean of  $\mu_E(x)$  and standard deviation of  $\sigma_E(x)$ , using KLE, it can be represented

$$E(x,\theta) = \mu_{E(x)} + \sigma_{E(x)} \sum_{i=1}^{\infty} \sqrt{\lambda_i} \phi_i(x) \xi_i(\theta)$$
 (12)

$$\begin{bmatrix} K_{00} & K_{01} & & & K_{0,P-2} & K_{0,P-1} \\ K_{10} & K_{11} & & & K_{1,P-2} & K_{1,P-1} \\ & \vdots & & \ddots & & \vdots \\ K_{P-2,0} & K_{P-2,1} & & K_{P-2,P-2} & K_{P-2,P-1} \\ K_{P-1,0} & K_{P-1,1} & & & K_{P-1,P-2} & K_{P-1,P-1} \end{bmatrix} \begin{bmatrix} U_0 \\ U_1 \\ \vdots \\ U_{P-2} \\ U_{P-1} \end{bmatrix} = \begin{bmatrix} F_0 \\ F_1 \\ \vdots \\ F_{P-2} \\ F_{P-1} \end{bmatrix}$$

### 4. Numerical implementation of incre- or the general strain increment, $d\epsilon(x,\theta)$ as follows: mental elastoplastic relationships

Based on the history of plastic deformations, the incremental solution is derived from the connection between a tiny stress increment and a little strain increment corresponding to the stress state.[39-43] In this part, first, the mechanics of the dissolving process is defined before rewriting the incremental relationships for an elastoplastic material in the form of a matrix. In the matrix form, the stress increment  $d\sigma(x,\theta)$  can be expressed by the elastic strain increment term  $d\epsilon^e(x,\theta)$  The stochastic stiffness matrix of a finite element is

$$k_i^{(e)}(\theta) = k_0^{(e)} + \sum_{i=1}^{\infty} k_i^{(e)} \xi_i(\theta)$$
 (13)

In the above formulas, the symbols have already been defined.

$$k_i^{(e)} = \sqrt{\lambda_i} \int_{\Omega} \phi_i(x) B^T D_0 B \, \mathrm{d}\Omega \tag{14}$$

Assuming that the load is certain, the equilibrium equation of the finite elements will be as follows:

$$\left[k_0^{(e)} + \sum_{i=1}^{\infty} k_i^{(e)} \xi_i(\theta)\right] U(\theta) = F$$
 (15)

The final equation of equilibrium will be:

$$\left(\sum_{i=0}^{\infty} K_i \xi_i(\theta)\right) \left(\sum_{i=0}^{\infty} U_i \psi_i(\theta)\right) - F = 0$$
 (16)

Finally, a limited number of terms of both expansions are retained. The term M in KLE and the term p in PCE lead to the residue of  $\in_{M,P}$ , which in the concept of mean squares must be minimized in order to obtain the optimal approximation of the exact solution  $U(\theta)$  by polynomial  $\psi_i(\theta)$ :

$$E[\in_{M,P}\psi_k]=0, k=0,1,2..., P-1$$
 (17)

After several algebraic operations in a system with N degrees of freedom with  $P = \frac{(M+p)!}{M!p!}$ , the linear system of equations with dimensions  $(N \times P) * (N \times P)$ 

$$\begin{bmatrix} U_{0} \\ U_{1} \\ \vdots \\ U_{P-2} \\ U_{P-1} \end{bmatrix} = \begin{bmatrix} F_{0} \\ F_{1} \\ \vdots \\ F_{P-2} \\ F_{P-1} \end{bmatrix}$$
(18)

$$\{d\sigma(x,\theta)\} = [C(x,\theta)]\{d\epsilon^{e}(x,\theta)\}$$

$$= [C(x,\theta)](\{d\epsilon(x,\theta)\} - \{d\epsilon^{P}(x,\theta)\}) \quad (19)$$

$$\{d\sigma(x,\theta)\} = [C^{ep}(x,\theta)]\{d\epsilon(x,\theta)\} \quad (20)$$

The increment of plastic strain  $\{d\epsilon^P(x,\theta)\}$  is expressed using a dependent rule as follows:

$$\{ d\epsilon^{P}(x,\theta) \} = d\lambda \frac{\partial f}{\partial \{ \sigma(x,\theta) \}}$$
 (21)

Where  $\frac{\partial f}{\partial \{\sigma(x,\theta)\}}$  is a gradient vector of the yield

function  $f(\sigma_{ij}(x,\theta); k(x,\theta))$ . The scalar function  $d\lambda$  is expressed as Eq. (22):

$$\mathrm{d}\lambda = \frac{L}{h} \tag{22}$$

Where L is the function of the loading criterion defined in Eq. (23):

$$L = \left\{ \frac{\partial f}{\partial \{\sigma(x,\theta)\}} \right\}^T [C(x,\theta)] \{ d\epsilon(x,\theta) \}$$
 (23)

The scalar function h is defined in Eq. (24):

$$h = \left\{ \frac{\partial f}{\partial \{\sigma(x,\theta)\}} \right\}^{T} [C(x,\theta)] \left\{ \frac{\partial f}{\partial \{\sigma(x,\theta)\}} \right\} + A^{'} \quad (24)$$

Where A' is:

$$A' = -\frac{dk(x,\theta)}{d\in} C \sqrt{\left\{\frac{\partial f}{\partial \{\sigma(x,\theta)\}}\right\}^T \left\{\frac{\partial f}{\partial \{\sigma(x,\theta)\}}\right\}}$$

$$\frac{\partial f}{\partial k(x,\theta)} \tag{25}$$

Where:

$$k(x,\theta) = \frac{\sigma_{yv}(x,\theta) + E_p(x,\theta)(\epsilon(x,\theta) - \epsilon^e(x,\theta))}{\sqrt{3}}$$

$$\to \frac{\mathrm{d}k(x,\theta)}{d\epsilon}$$

$$= \frac{E_p(x,\theta)}{\sqrt{3}}$$
(26-a)

$$C = \sqrt{\frac{2}{3}} \tag{26-b}$$

$$\frac{\partial f}{\partial k(x,\theta)} = -2k(x,\theta) = -\frac{2}{\sqrt{3}}\sigma_{yv}(x,\theta) \tag{26-c}$$

And for a material with a hardening model, we will have bilinear:

$$E_p(x,\theta) = \frac{E(x,\theta)E_T(x,\theta)}{E(x,\theta) - E_T(x,\theta)}$$
(27)

Finally, the elastoplastic hardness matrix  $[C^{ep}(x,\theta)]$  is:

$$[C^{ep}(x,\theta)] = [C(x,\theta)] - \frac{[C(x,\theta)] \left\{ \frac{\partial f}{\partial \{\sigma(x,\theta)\}} \right\} \left\{ \frac{\partial f}{\partial \{\sigma(x,\theta)\}} \right\}^T [C(x,\theta)]}{\left\{ \frac{\partial f}{\partial \{\sigma(x,\theta)\}} \right\}^T [C(x,\theta)] \left\{ \frac{\partial f}{\partial \{\sigma(x,\theta)\}} \right\} + A'}$$
(28)

For the plane stress state, when the von Mises yield criterion is used,  $\left\{\frac{\partial f}{\partial \{\sigma(x,\theta)\}}\right\}$  is obtained as follows:

$$\left\{ \frac{\partial f}{\partial \{\sigma(x,\theta)\}} \right\} = \left\{ \begin{array}{c} \frac{2\sigma_{11}(x,\theta) - \sigma_{22}(x,\theta)}{3} \\ \frac{2\sigma_{22}(x,\theta) - \sigma_{11}(x,\theta)}{3} \\ 2\sigma_{12}(x,\theta) \end{array} \right\}$$
(29)

Stress calculations will be performed for all Gaussian points. In the following, the calculations will be considered for only one Gaussian point. In step (m+1), the stresses  ${}^m\{(x,\theta)\sigma\}$  and the strains  ${}^m\{\epsilon(x,\theta)\}$  in step m are specified, and the hardening parameters  $({}^mk(x,\theta)$  and  ${}^m{}_p(x,\theta))$  are also calculated at the end of the step m. For a typical iteration step, i-th approximate displacement  ${}^{m+1}\{U\}^{(i)}$  is obtained from the (m+1)-th increment of the load. The strain and strain increment corresponding to this displacement at the Gaussian point will be as follows:

$$^{m+1}\{\epsilon\}^{(i)} = [B]^{m+1}\{U\}^{(i)}$$
 (30)

$$\{\Delta\epsilon(x,\theta)\} = {}^{m+1}\{(x,\theta)\epsilon\}^{(i)} - {}^m\{\epsilon(x,\theta)\}$$
 (31)

First, assuming that the behavior of materials during the strain increment calculated in Eq. (31) remains in the elastic range, the elastic stress increment equivalent to this strain increment is calculated as follows:

$$\{\Delta \sigma^e(x,\theta)\} = [C(x,\theta)] \{\Delta \epsilon(x,\theta)\}$$
 (32)

Assuming that at the end of the m-th increment, the stress state at the Gaussian point satisfies the elastic state conditions  $f(^m\{\sigma(x,\theta)\}; ^mk(x,\theta)) < 0$  and in the increment (m+1) enters an elastoplastic state  $f(^m\{\sigma\} + \{\Delta\sigma^e\}; ^mk) > 0$ . Therefore, there is a scaling factor (Fig. 2) "r" for which it will be:  $f(^m\{\sigma(x,\theta)\} + r\{\Delta\sigma^e(x,\theta)\}; ^mk(x,\theta)) = 0$ . Then, the strain will be divided into two parts  $r\{\Delta\epsilon(x,\theta)\}$  and  $(1-r)\{\Delta\epsilon(x,\theta)\}$ . The first part deals with the fully elastic response of materials, while the second part is related to the response of elastoplastic materials. Therefore, the stress increment can be obtained from the following integral as follows:

$$\{\Delta\sigma(x,\theta)\} = \int_{m_{\{\epsilon(x,\theta)\}}}^{m+1_{\{\epsilon(x,\theta)\}}} [C(x,\theta)](\{d\epsilon(x,\theta)\})$$

$$-\{d\epsilon^{P}(x,\theta)\})$$

$$= \int_{m_{\{\epsilon(x,\theta)\}}}^{m_{\{(\kappa,\theta)\epsilon\}+r_{\{\Delta\epsilon(x,\theta)\}}}} [C(x,\theta)]\{d\epsilon(x,\theta)\}$$

$$+ \int_{m_{\{\epsilon(x,\theta)\}+r_{\{\Delta\epsilon(x,\theta)\}}}}^{m_{\{\epsilon(x,\theta)\}+r_{\{\Delta\epsilon(x,\theta)\}}}} [C(x,\theta)]$$

$$-\{d\epsilon^{P}(x,\theta)\}$$

$$-\{d\epsilon^{P}(x,\theta)\}$$

$$-\{d\epsilon^{P}(x,\theta)\}$$

$$-\{d\epsilon^{P}(x,\theta)\}$$

$$+ \int_{m_{\{\epsilon(x,\theta)\}+r_{\{\Delta\epsilon(x,\theta)\}}}}^{m_{\{\epsilon(x,\theta)\}+r_{\{\Delta\epsilon(x,\theta)\}}}} [C(x,\theta)]$$

$$-\{d\epsilon(x,\theta)\} - \{d\epsilon^{P}(x,\theta)\}$$

$$-\{d\epsilon^{P}(x,\theta)\}$$

Finally, the stress corresponding to  $^{m+1}\{U\}^{(i)}$  will 4.2. Calculation of the scale factor "r" be obtained as follows:

$$^{m+1} \{ \sigma(x,\theta) \}^{(i)} = ^{m} \{ \sigma(x,\theta) \} + \{ \Delta \sigma(x,\theta) \}$$
 (35)

#### 4.1. Determination of the loading state

The first step in stress calculations is to determine the loading state of a Gaussian point; in other words, to determine whether the Gaussian point is in the state corresponding to the strain increment  $(\{\Delta \epsilon(x,\theta)\})$  in the plastic loading state, the elastic state, or in the loading state. Only in situations when the plastic load is dominating, the elastoplastic relations are applied. The governing ties are more flexible in other circumstances. The state of materials is analyzed in two entirely different scenarios for this aim. The first state corresponds to the Gaussian point being in an elastic state at the conclusion of step m, whereas the second state relates to the Gaussian point being in an elastoplastic state. If the end point of the m-th Gaussian point is in the elastic state,  $f(^m\{\sigma(x,\theta)\}; ^mk(x,\theta)) < 0$ , assuming that it is created by applying the strain increment, the state of the Gaussian point remains in the elastic state, and the corresponding stress increment is calculated using Eq. (32). According to the stress obtained based on the above hypothesis, the state of the Gaussian point is examined. If the yield criterion confirms the correctness of the initial hypothesis that the position of the Gaussian point is in the elastic state,  $f(^m \{\sigma(x,\theta)\} + \{\Delta \sigma^e(x,\theta)\}; ^m k(x,\theta)) < 0$ at the end of increment (m + 1), all stress calculations at the Gaussian point can be calculated based on elasticity relations. However, if the study of the yield criterion indicates that the materials yield,  $f(^{m}\{\sigma(x,\theta)\} + \{\Delta\sigma^{e}(x,\theta)\}; ^{m}k(x,\theta)) > 0$ , the calculation of scale factor "r" of the fully elastic strain must be separated from the elastoplastic strain. Then, the stress increment in the elastic part is calculated using the calculated elasticity relations, and the governing elastoplastic relationships are used for calculating the stress increment in the elastoplastic part.

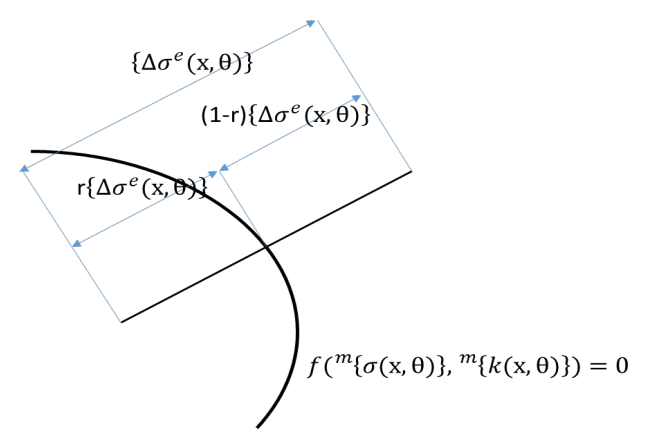


Fig. 2. Schematic representation of the scale factor rto separate the elastic part from the elastoplastic part.

The scale factor "r" is shown schematically in Fig. 2. To obtain the scale factor, Eq. (36) should be solved. Eq. (36) can be solved both analytically and numerically. If the yield equation is expressed simply based on the invariables, the solution can be analytically obtained; otherwise it is necessary to use numerical methods to solve Eq. (36).

$$f(^{m}\lbrace \sigma(x,\theta)\rbrace + r\lbrace \Delta\sigma^{e}(x,\theta)\rbrace ; ^{m}k(x,\theta)) = 0$$
 (36)

Due to the simplicity of the equation form, the von Mises criteria may be solved both analytically and numerically. As a result, both analytical and numerical approaches to obtaining the scale factor for the von Mises yield criterion will be described in this section. However, it should be noted that the iterative procedure is used to determine the scale factor of numerical techniques in general. With the isotropic hardening model, the usual equations for the von Mises yield are:

$$f(\lbrace \sigma(x,\theta)\rbrace, k(x,\theta)) = \frac{1}{2} \lbrace S(x,\theta)\rbrace^T \lbrace S(x,\theta)\rbrace - k^2 (\epsilon_P(x,\theta))$$
(37)

Where  $\{S(x,\theta)\}\$  is the vector of deviator stresses defined as follows:

$$\{S(x,\theta)\}^T = \{S_x(x,\theta); S_y(x,\theta); S_z(x,\theta); S_{yz}(x,\theta); S_{zx}(x,\theta); S_{xy}(x,\theta)\}$$
(38)

The increment of the deviator stress is also defined as follows:

$$\{\Delta S(x,\theta)\}^{T} = \{\Delta S_{x}(x,\theta), \Delta S_{y}(x,\theta), \Delta S_{z}(x,\theta), \Delta S_{yz}(x,\theta), \Delta S_{zx}(x,\theta), \Delta S_{xy}(x,\theta)\}$$
(39)

To analytically solve Eq. (36) based on deviator stresses and the increment of deviator stresses, we have:

$$f(^{m}\{\sigma(x,\theta)\}+r\{\Delta\sigma^{e}(x,\theta)\},^{m}k(x,\theta))$$

$$=\frac{1}{2}(^{m}\{S(x,\theta)\}+r\{\Delta S(x,\theta)\})^{T}$$

$$(^{m}\{S(x,\theta)\}+r\{\Delta S(x,\theta)\})-^{m}k^{2}(\epsilon_{P}(x,\theta))$$

$$=0$$
(40)

$$\frac{1}{2}r^{2}\{\Delta S(x,\theta)\}^{T}\{\Delta S(x,\theta)\} + r^{m}\{S(x,\theta)\}^{T}\{\Delta S(x,\theta)\} + \frac{1}{2}^{m}\{S(x,\theta)\}^{Tm}\{S(x,\theta)\} - m^{m}k^{2}(\epsilon_{P}(x,\theta)) = 0$$
(41)

Hence, the scale factor r is obtained by solving Eq.

$$\frac{1}{2}r^{2}\{\Delta S(x,\theta)\}^{T}\{\Delta S(x,\theta)\} + r^{m}\{S(x,\theta)\}^{T}\{\Delta S(x,\theta)\} + \frac{1}{2}^{m}\{S(x,\theta)\}^{Tm}\{S(x,\theta)\} - mk^{2}(\epsilon_{P}(x,\theta)) = 0 \tag{42}$$

To numerically solve an iterative process until we solution will be presented in Eq. (43). reach the desired error rate, the general process of this

$$r^{(i)} = \frac{f(^{m}\{\sigma(x,\theta)\}, ^{m}k(x,\theta))}{f(^{m}\{\sigma(x,\theta)\}, ^{m}k(x,\theta)) - f(^{m}\{\sigma(x,\theta)\} + \{\Delta\sigma^{e}(x,\theta)\}, ^{m}k(x,\theta))}$$

$$r^{(i+1)} = r^{(i)} - \frac{f(^{m}\{\sigma(x,\theta)\} + r^{(i)}\{\Delta\sigma^{e}(x,\theta)\}, ^{m}k(x,\theta))}{f(^{m}\{\sigma(x,\theta)\} + r^{(i-1)}\{\Delta\sigma^{e}(x,\theta)\}, ^{m}k(x,\theta)) - f(^{m}\{\sigma(x,\theta)\} + r^{(i)}\{\Delta\sigma^{e}(x,\theta)\}, ^{m}k(x,\theta))} (r^{(i-1)} - r^{(i)})$$

$$(43)$$

#### 4.3. Integration Techniques

The algorithms used to integrate Eq. (33) or (34) can be divided into two categories: One group is based on explicit techniques and the other group is based on implicit techniques. For both types, to achieve the required accuracy in the integration process, the elastoplastic strain increment can be divided into an appropriate number of n, which is called sub-increment,  $\{\Delta \widetilde{\in} (x,\theta)\}.$ 

$$\{d\epsilon(x,\theta)\} = \{\Delta \widetilde{\in} (x,\theta)\} = \frac{(1-r)\{\Delta \in (x,\theta)\}}{n}$$
 (44)

Forward stresses are estimated from one strain subincrement to the next, if an explicit procedure is employed, such as the Euler forward method. The stresses at the end of each sub-increment are computed again, if an implicit approach is employed, such as the Euler backward method. Hence, in this case, there are two iterative loops in solving nonlinear equations, one is the iteration loop of equilibrium equations, and the other is during the integration process to evaluate the accuracy of stresses. In this section, we will only discuss some details of the explicit Euler forward method. For each sub-increment,  $\{\Delta \widetilde{\in} (x,\theta)\}$ , the explicit method includes the following steps:

Step 1: Determine the plastic strain increment using  $\{\Delta \tilde{\epsilon}^p\}$  with a suitable algorithm and determine the effective plastic strain increment  $\Delta \widetilde{\in}_p$ .

$$\{\Delta \widetilde{\epsilon}^p(x,\theta)\} = \frac{(1-r)}{n} \frac{L}{h} \left\{ \frac{\partial f}{\partial \{\sigma(x,\theta)\}} \right\}$$
 (45)

Step 2: Calculate the stress sub-increment  $\{\Delta \widetilde{\sigma}(x,\theta)\}\$ 

$$\{\Delta \widetilde{\sigma}(x,\theta)\} = [C(x,\theta)](\{\Delta \widetilde{\epsilon}(x,\theta)\} - \{\Delta \widetilde{\epsilon}^p(x,\theta)\})$$
(46)

Step 3: Update the stress, strain and hardening parameters:

$$\{\sigma(x,\theta)\} \leftarrow \{\sigma(x,\theta)\} + \{\Delta \widetilde{\sigma}(x,\theta)\} 
\{ \in (x,\theta)\} \leftarrow \{\epsilon(x,\theta)\} + \{\Delta \widetilde{\in}(x,\theta)\} 
\{ \in^{P}(x,\theta)\} \leftarrow \{ \in^{P}(x,\theta)\} + \{\Delta \widetilde{\epsilon}^{p}(x,\theta)\} 
\epsilon_{P}(x,\theta) \leftarrow \epsilon_{P}(x,\theta) + \Delta \widetilde{\in}_{p}(x,\theta), k \leftarrow k(\epsilon_{P}(x,\theta))$$

$$(47)$$

#### 4.4. Modification of the Increments to Satisfy Compatibility Conditions

Compatibility conditions df = 0 must be met in a plastic loading process. However, since many approximations are used in a numerical solution, the compatibility conditions are often not met. Adding a strain sub-increment to the next load state results in:

$$f(\lbrace \sigma(x,\theta)\rbrace;\epsilon_P(x,\theta))\neq 0$$
 (48)

In other words, the stress is not on the next yield surface and moves away from the yield surface. Such a stress deviation accumulates from the vield surface and leads to very important errors for solving nonlinear equations. As a result, the stress vector must be changed to meet the compatibility requirements. Adding a correction vector in the direction of the normal yield surface vector to the stress vector is a common way to do so.

$$\{\delta\sigma(x,\theta)\} = a \left\{ \frac{\partial f}{\partial \{\sigma(x,\theta)\}} \right\}$$

$$a = \frac{-f(\{\sigma(x,\theta)\}, k(x,\theta))}{\left\{ \frac{\partial f}{\partial \{\sigma(x,\theta)\}} \right\}^T \left\{ \frac{\partial f}{\partial \{\sigma(x,\theta)\}} \right\}}$$
(49)

Finally, the modified stress vector will be obtained:

$$\{\sigma(x,\theta)\} \leftarrow \{\sigma(x,\theta)\} + \{\delta\sigma(x,\theta)\} \tag{50}$$

#### 4.5. Formulation of the Structures with Nonlinear Materials in SSFEM:

To use SSFEM for solving uncertain structures with nonlinear materials, first, by using the operators of this method and selecting the appropriate number of terms from KLE and PCEs, the input random variables and solution are modeled. Then, the process of solving the stiffness matrix is formed and assuming that the behavior of the materials is linear, the problem begins to be solved. In each increment, before a solution subincrement is completed, the stress state at the Gaussian points is checked so that if the material yielding criteria are activated, the operators of the plastic condition applications modify the stresses and, consequently, the solutions are corrected. This process continues until the problem is completely solved and the desirable solution is achieved.

#### 4.6. Structural Reliability Analysis Based on Spectral Finite Element Method

In the sense of structural reliability, the probability of failure occurs when the load and material properties are random variables (X), and structural failure can be estimated using a finite state function (g(x)) defined for the structure response. The failure probability is then calculated using the multiple integral defined in the failure domain  $Df = \{g(x) \leq 0\}$  as follows [33]:

$$P_f = \operatorname{prob}[g(x) \le 0] = \int_{Df} f(x) \, \mathrm{d}x \tag{51}$$

Where f(x) is PDF x and prob is a measure of probability. Since Eq. (51) is difficult to solve in most engineering problems, various numerical methods were proposed for these problems. Since the output of stochastic spectral finite elements is a structural stochastic response vector, it could be easy to calculate the PDF and CDF of the responses and the probability of structural failure using MCS. The probability of failure can be approximated as follows:

$$P_f = \frac{n}{N} \tag{52}$$

Where n is the number of samples for  $g(x) \leq 0$ , and Ns is the total number of samples. The reliability index  $(\beta)$  in MCS is defined as follows:

$$\beta = -\Phi^{-1}(P_f) \tag{53}$$

Where  $\Phi$  is the CDF of normal standard.

#### 5. Numerical Examples

#### 5.1. Example 1: A Square Plate

Fig. 3 shows a plate in the plane stress mode with dimensions of 160 \* 160 \* 2mm, zero material density and Poisson's coefficient of 0.3 under four concentrated horizontal loads p1 in three nodes, 2,3 and 4 and three concentrated vertical loads p2 in nodes 10,15 and 20 that, the specifications of the loads are listed in Table 1. The support is between rigid nodes 1 to 21. For analysis, loading, modulus of elasticity E (Fig. 4) and yield stress S are considered as random fields with mean and standard deviation  $\sigma$ . All three parameters are defined based on Eq. (54) using the two-dimensional exponential function. bx and by are correlation lengths, which

are assumed to be equal to 160 in both directions, and for a KLE with 4 terms, eigenvalues and eigenvectors are shown in Fig. 5 and Fig. 6. In this case, the maximum acceptable displacement is 6mm. In this example, by changing the number of M and p, the effect of increasing and decreasing the number of KLE terms and the order of PCE on the accuracy of the results are evaluated.

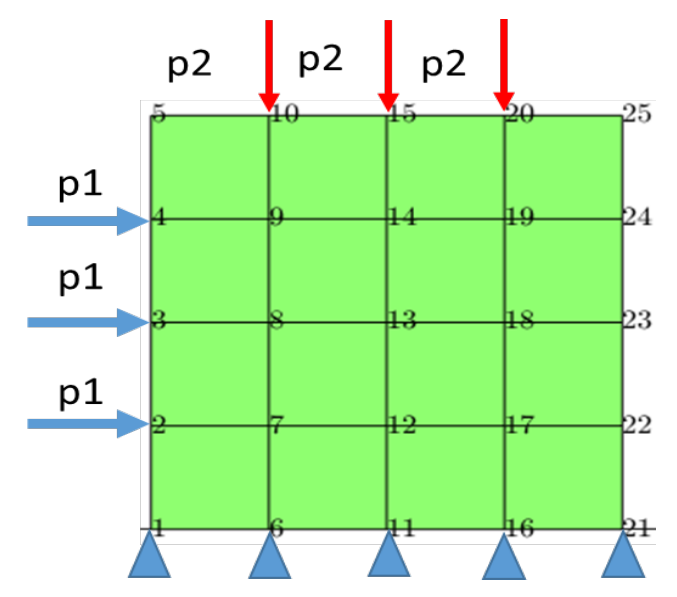
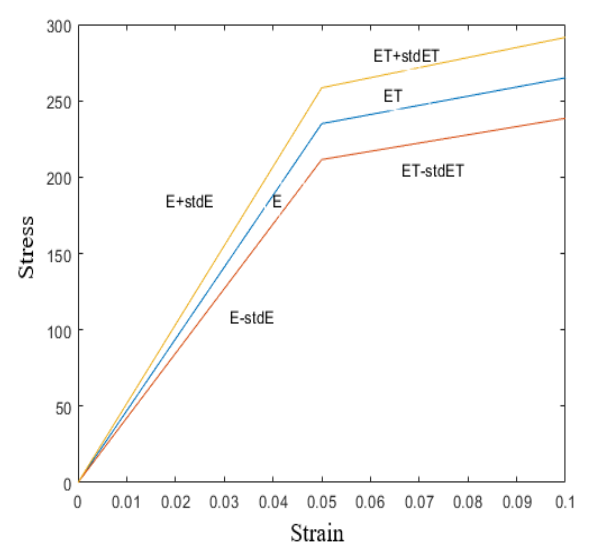


Fig. 3. The structure examined in example 1.



**Fig. 4.** Modulus of elasticity of the materials in examples 1 and 2.

Table 1
Structure input specifications of example 1.

Value	Parameter	Value	Parameter	Value	Parameter	Value	Parameter
25	Nodes	235MPa	$\mu S$	20GPa	$\mu \mathrm{ET}$	20000N	$\mu$ p1
16	Elements	23.5MPa	$\sigma S$	2GPa	$\sigma \mathrm{ET}$	2000N	$\sigma$ p1
$40 \text{mm} \times 40 \text{mm}$	Mesh size	160	bx	200GPa	$\mu { m E}$	30000N	$\mu \mathrm{p}2$
		160	by	20GPa	$\sigma \mathrm{E}$	3000N	$\sigma$ p2

$$C(X_1, X_2) = \exp\left(-\frac{|x_1, x_2|}{b_x} - \frac{|y_1, y_2|}{b_y}\right)$$
 (54)

The mean displacements and stresses and standard deviations resulted from NSSFEM can be seen in Fig. ??. By examining the results obtained from the proposed method and comparing these data with the outputs of the Monte Carlo method (10,000 samples were evaluated in both examples), the accuracy of the proposed solution was very favorable due to the reduction of computation time. Figs. 7 and 8 provide a comparison between the PDFs as well as the CDFs obtained for vertical displacement at node 25 and the accuracy

based on different Ms and ps. Based on the results presented in these figures, it can be found that the effect of increasing the M term is more than p in achieving the desirable result. On the other hand, M has an effect on the accuracy of the obtained values, and p has a very effective effect on the scatter of responses. The accuracy of the findings is high, with an error rate of less than 3%. Fig. 9 shows the relationship between the mean displacement values produced using the Monte Carlo approach and NSSFEM. Table 2 shows the results of the NSSFEM and MCS techniques for the chance of failure and computation time.

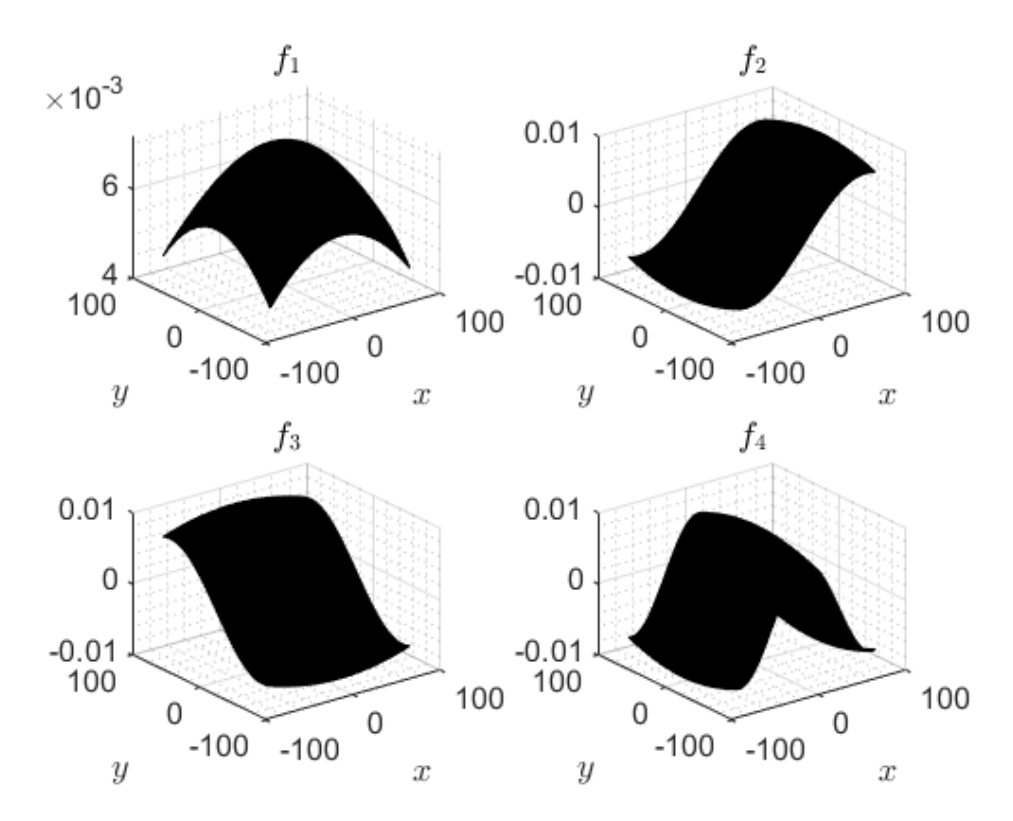


Fig. 5. Eigenvalues for 4 KLE terms in 2 dimensions.

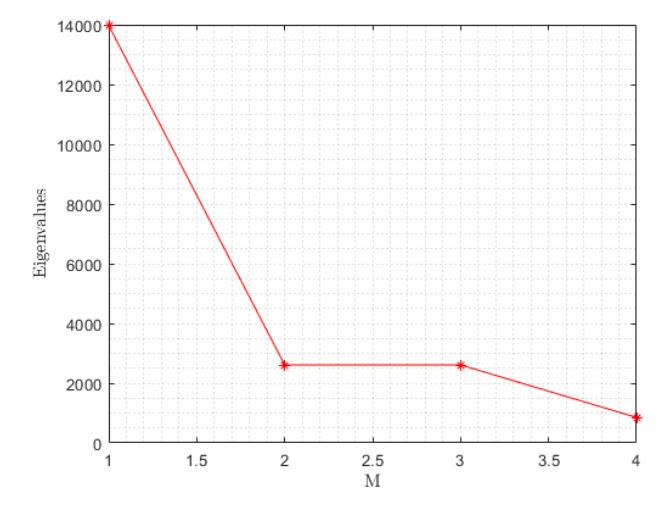


Fig. 6. Eigenvectors for 4 KLE terms in 2 dimensions.

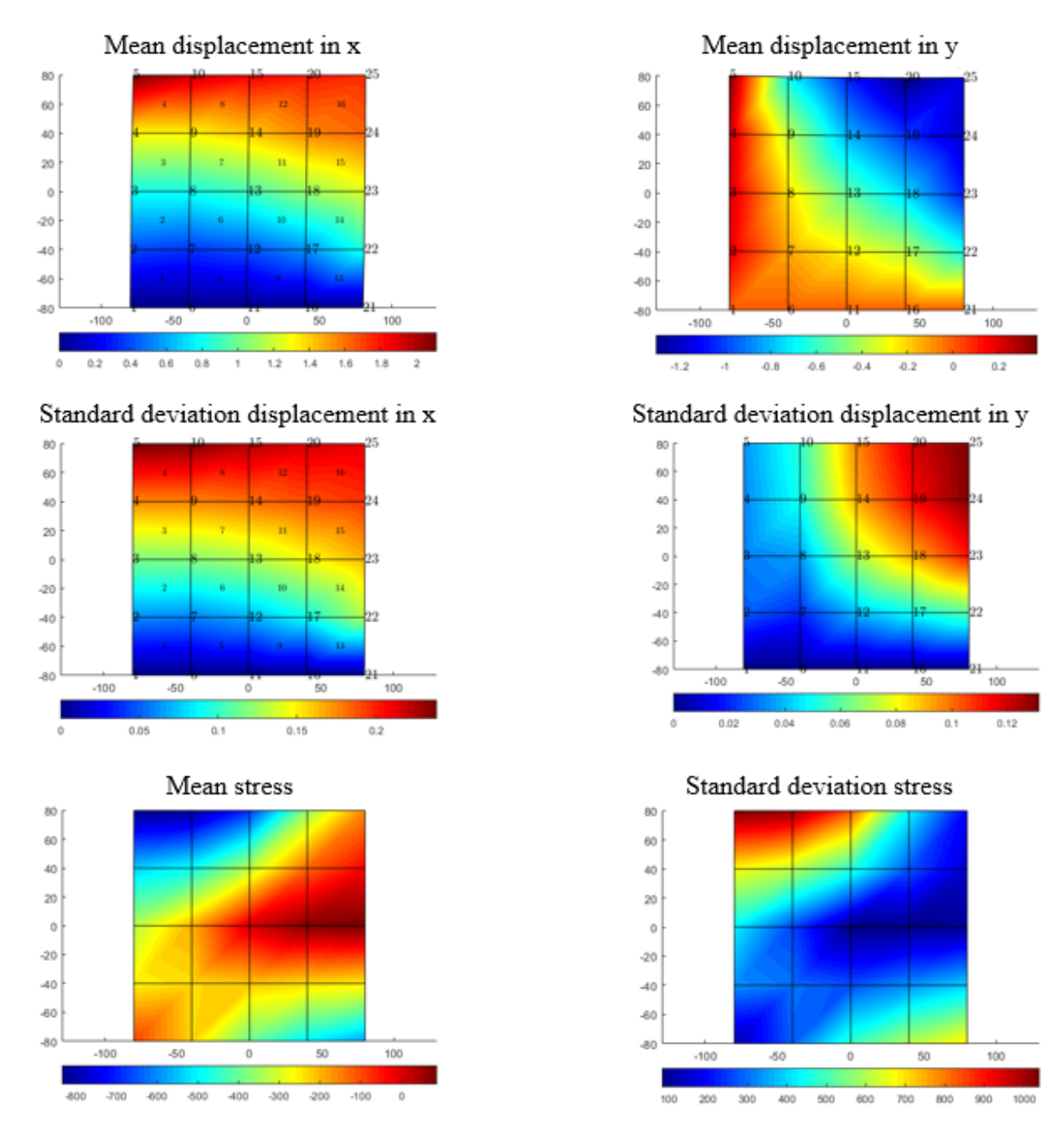
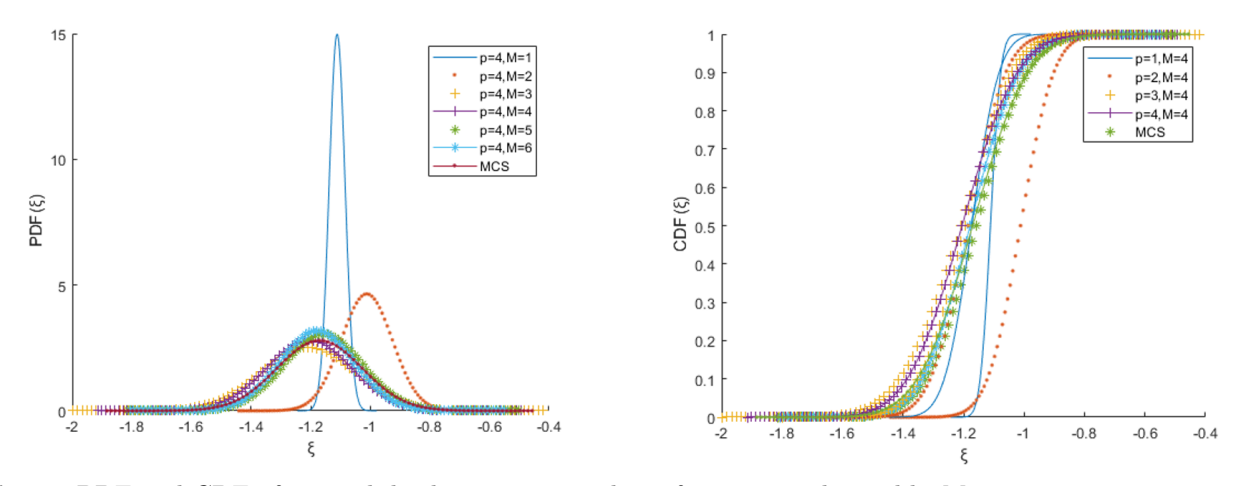
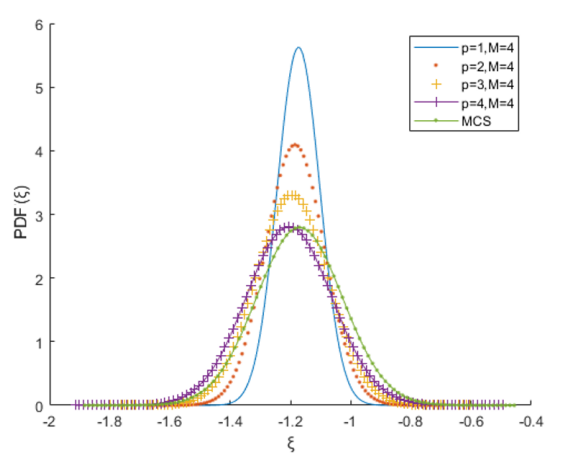
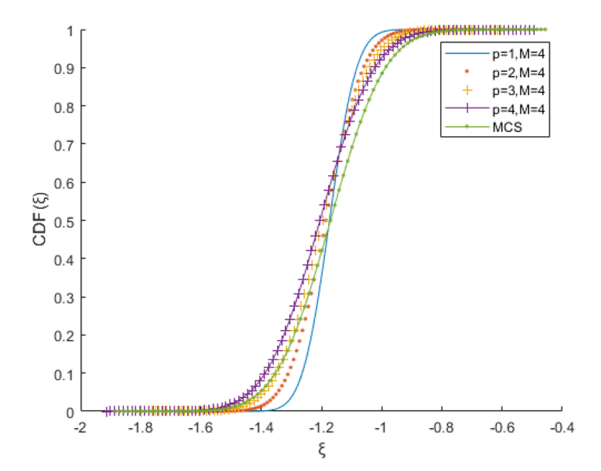


Fig. 7. Mean and standard deviation of displacement and stress in the structure example 1.



**Fig. 8.** PDF and CDF of vertical displacement at node 25 for p=4 and variable Ms.





**Fig. 9.** PDF and CDF of vertical displacement at node 25 for M=4 and variable p.

 ${\bf Table~2} \\ {\bf Probability~of~failure~and~structural~analysis~time~of~example~1}.$ 

Time (sec)	β	Pf	Case
17362	2.2058	0.0137	MCS
1273	2.2286	0.01292	NSSFEM

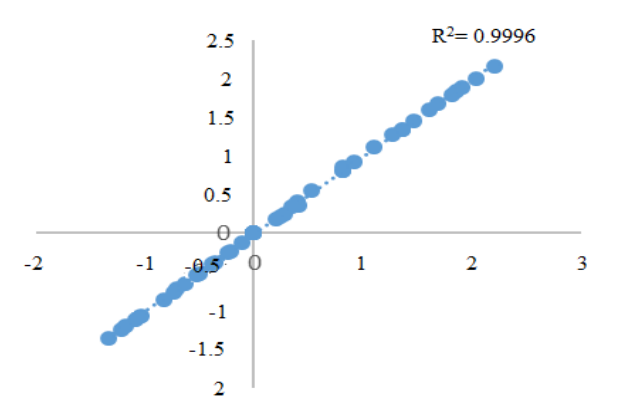


**Fig. 10.** Correlation between mean displacement values obtained from Monte Carlo method and SSFEM  $M=4,\ p=3.$ 

## 5.2. Example 2: A square plate with a central cut-out

Fig. 13 shows a square plate with a central cut-out with three different meshings in the plane stress mode with dimensions of 120\*120\*2mm. The density of materials is assumed to be zero and the Poisson's ratio to be 0.3. Structures under a wide vertical load q, three concentrated horizontal loads p1, and two concentrated vertical loads p2, where the locations of the

loads in each mesh were shown in Table 3, and the load specifications are presented in Table 4. The location of the joint support for each mesh is given in Table 3. For analysis of loading, modulus of elasticity E (Fig. 4) and yield stress S are considered as random fields with a mean and standard deviation  $\sigma$ . All three parameters are defined according to Eq. (54) using the two-dimensional exponential function. bx and by are correlation lengths assumed to be equal to 120 in both directions, and eigenvalues and eigenvectors for a KLE with 4 terms are displayed in Figs. 10 and 11.

In this case, the reliability analysis is performed using type 3 meshing, and a maximum acceptable displacement of 10mm is considered.

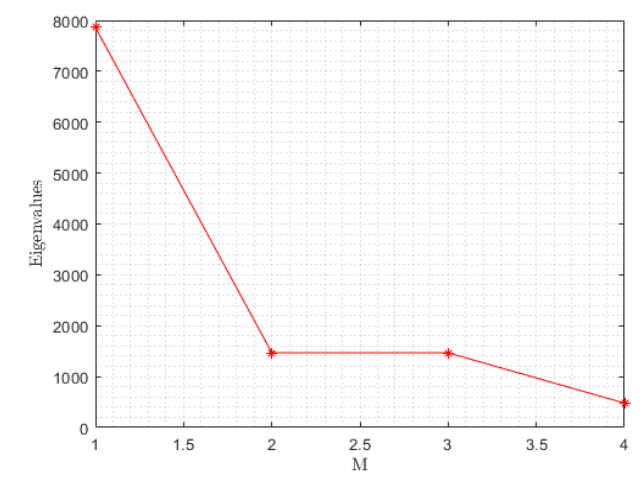


**Fig. 11.** Eigenvalues for 4 KLE terms in 2 dimensions for example 2.

Table 3
Meshing specifications and location of loads and supports in each meshing in example 2.

		1.1	0 1			
location of loads	location of loads	location of loads	Mesh	Number of	Number of	Mesh
q	p2  (nodes)	p1  (nodes)	size	nodes	elements	
Between nodes4-16	4,16	2, 3,4	$40\text{mm} \times 40\text{mm}$	16	9	Mesh1
Between nodes7-48	7,48	3, 5,7	$20\mathrm{mm}{\times}20\mathrm{mm}$	48	32	Mesh2
Between nodes13-160	13,160	13, 9,5	$10\mathrm{mm}{\times}10\mathrm{mm}$	160	128	Mesh3

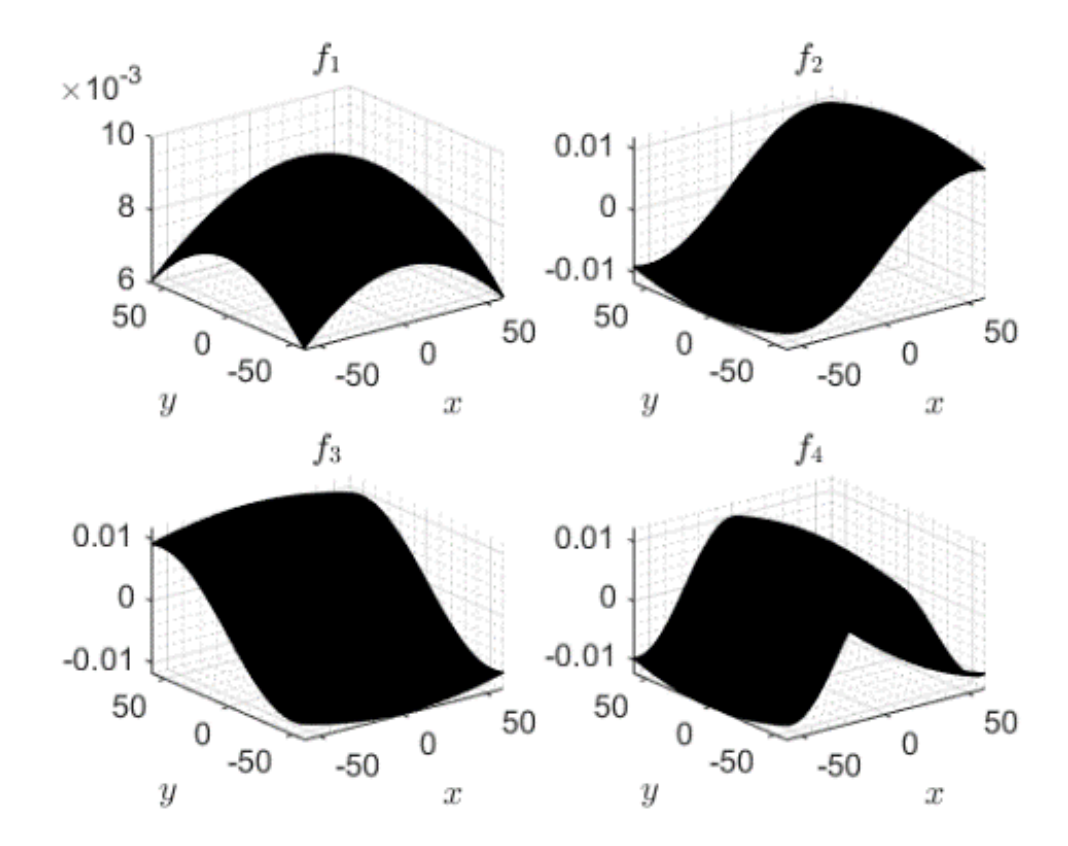


Fig. 12. Eigenvectors for 4 KLE terms in 2 dimensions for example 2.

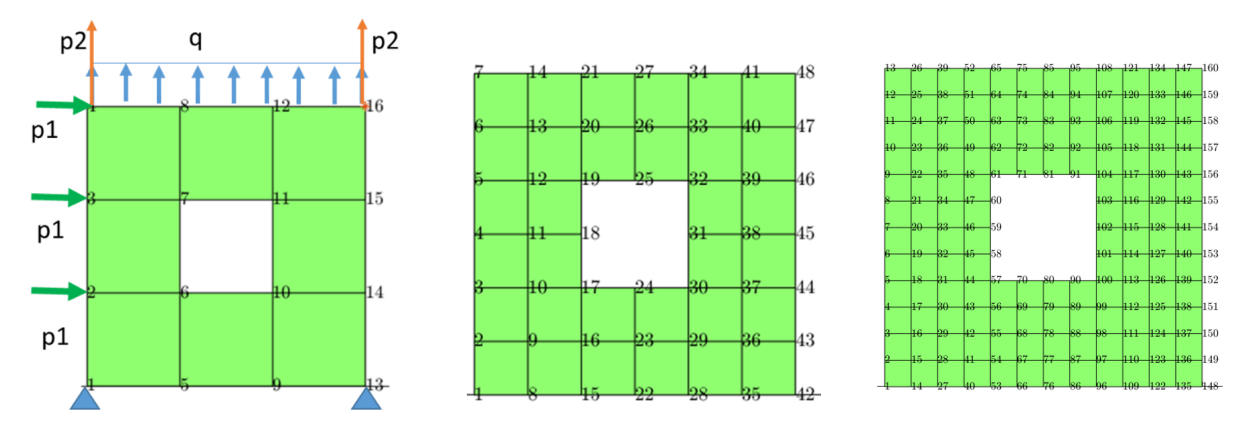


Fig. 13. Structural meshing of example 2.

Table 4
Structural input data of example 2.

Value	Parameter	Value	Parameter	Value	Parameter
100GPa	$\mu \ \mathrm{ET}$	1000N	$\mu p2$	$200\mathrm{N/mm}$	$\mu q$
10GPa	$\mathrm{ET}\sigma$	100N	$\sigma p2$	$20\mathrm{N/mm}$	$q\sigma$
235MPa	$\mu$ S	200GPa	$\mu E$	6~000N	$\mu p1$
23.5MPa	$\sigma S$	20GPa	$\mathrm{E}\sigma$	600N	$\sigma p1$

Three different sizes of meshing are utilized in this example to demonstrate how to achieve the desired solution and the impact of meshing dimensions. The findings were produced for varying M and p using two

forms of meshing 1 and 2 and compared to the values acquired using the Monte Carlo approach (Figs. 13-20). By viewing the PDF and CDF diagrams (Figs. 13, 14-16, and 18-20) obtained for the displacements, it can

be seen that by increasing the KL and PCE terms, the accuracy of the results is increased to the point that in both meshings with p=4, M=4, the mean value and standard deviation of displacement in the nodes with an error percentage of less than 4% correspond to the values obtained from Monte Carlo (Figs. 16, 20, and 23). For the third meshing, only p=4, M=4 were used in modeling the probabilistic parameters, the results of which can be observed in Figs. 21, 22, and 23. Fig. 23

shows the correlation between the outputs of MCS and NSSFEM, which can clearly show the resultant consistency. In this example, the mean error is less than 4%. Mean displacements and stresses and standard deviations obtained from NSSFEM can be seen in Figs. 13, 17, and 21 for all three types of meshing. The values obtained for the probability of failure as well as the duration of calculations of both NSSFEM and MCS are presented in Table 5.

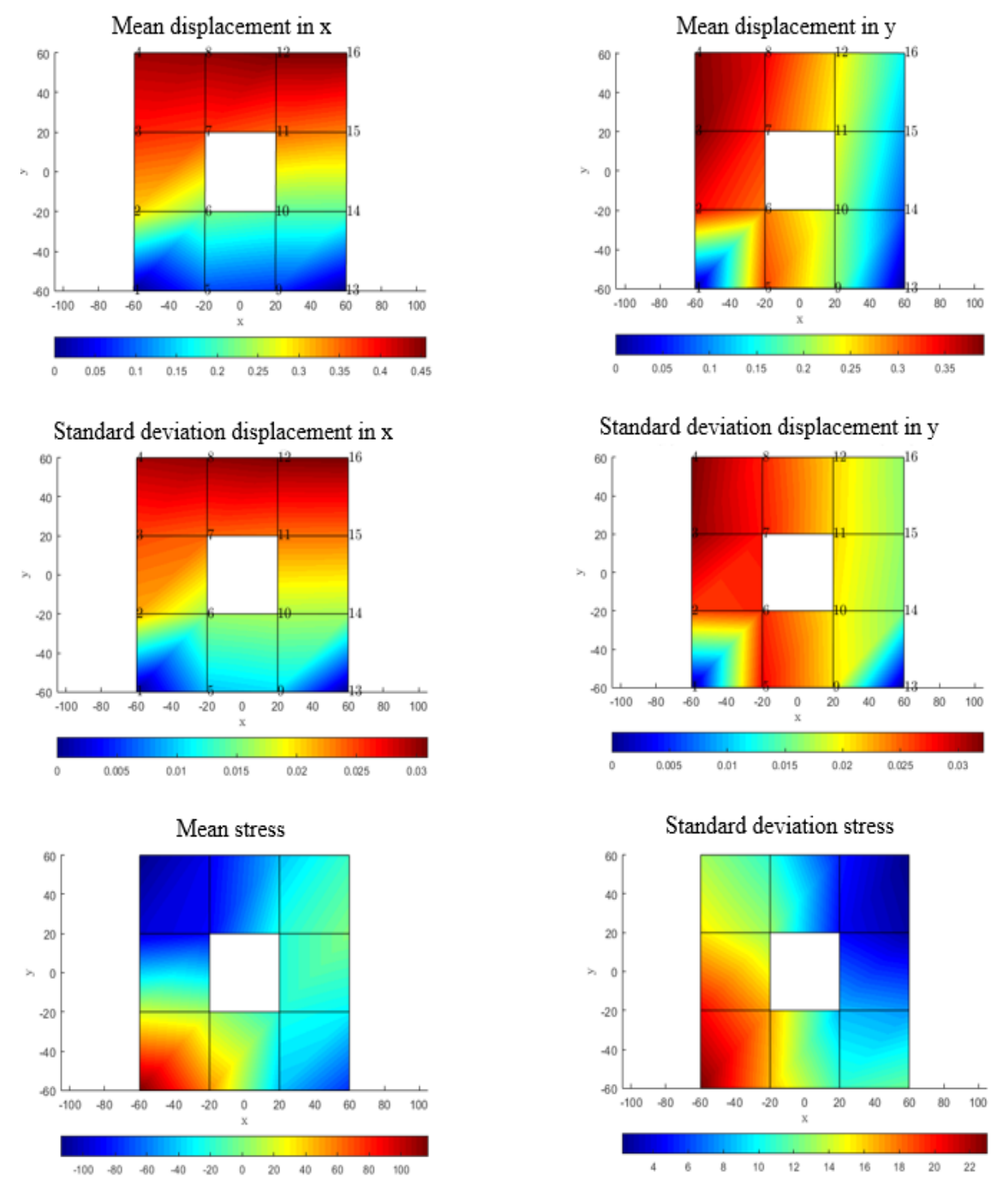


**Fig. 14.** Mean and standard deviation of displacement and stress in the structure of example 2, meshing No. 1.

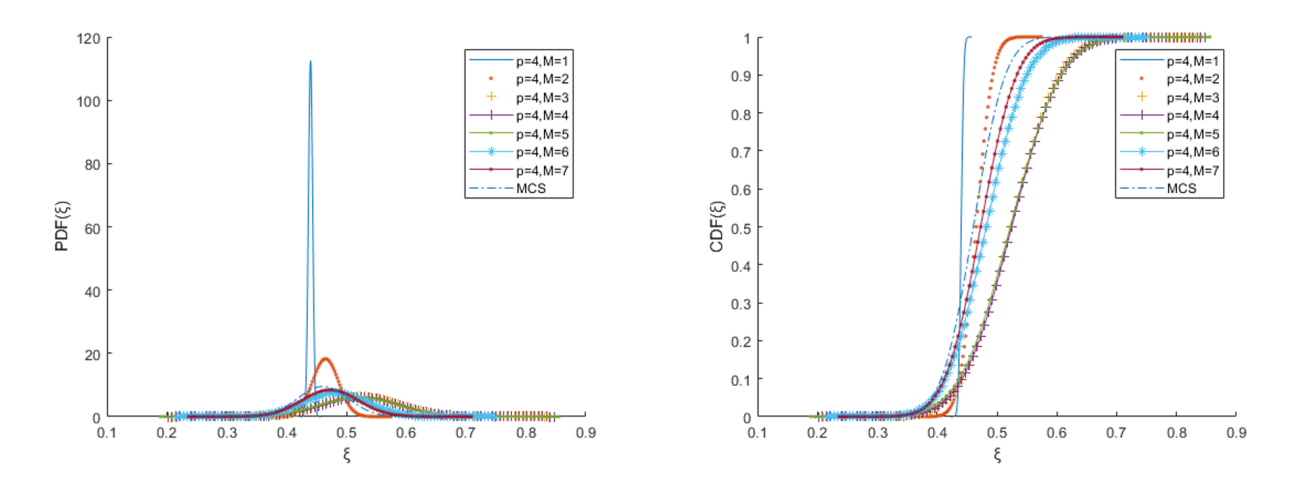


**Fig. 15.** PDF and CDF of horizontal displacement at node 16 for p=4 and variable Ms.

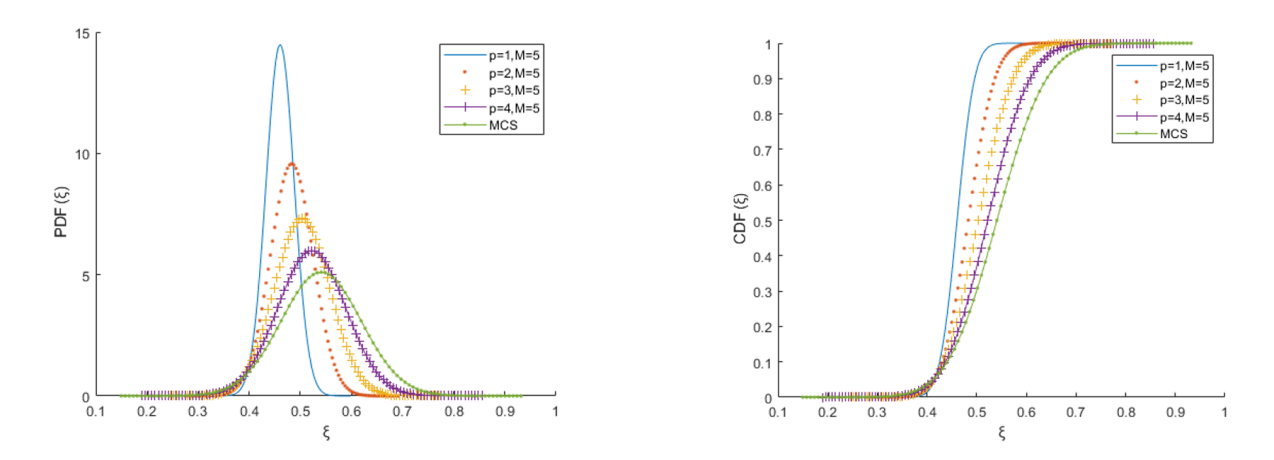


**Fig. 16.** PDF and CDF of horizontal displacement at node 16 for M=5 and variable p.

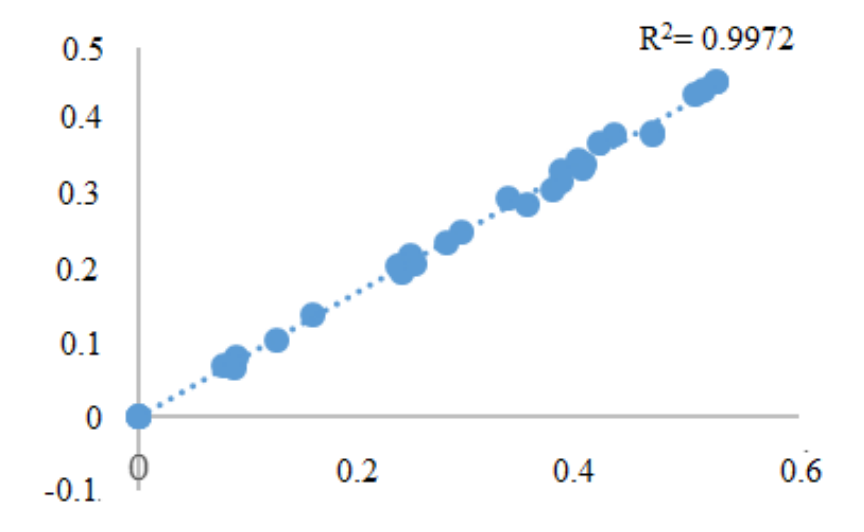


Fig. 17. Correlation between the mean displacement values obtained for meshing 1 of example 2 of the Monte Carlo method and the SSFEM  $M=4,\,p=4.$ 

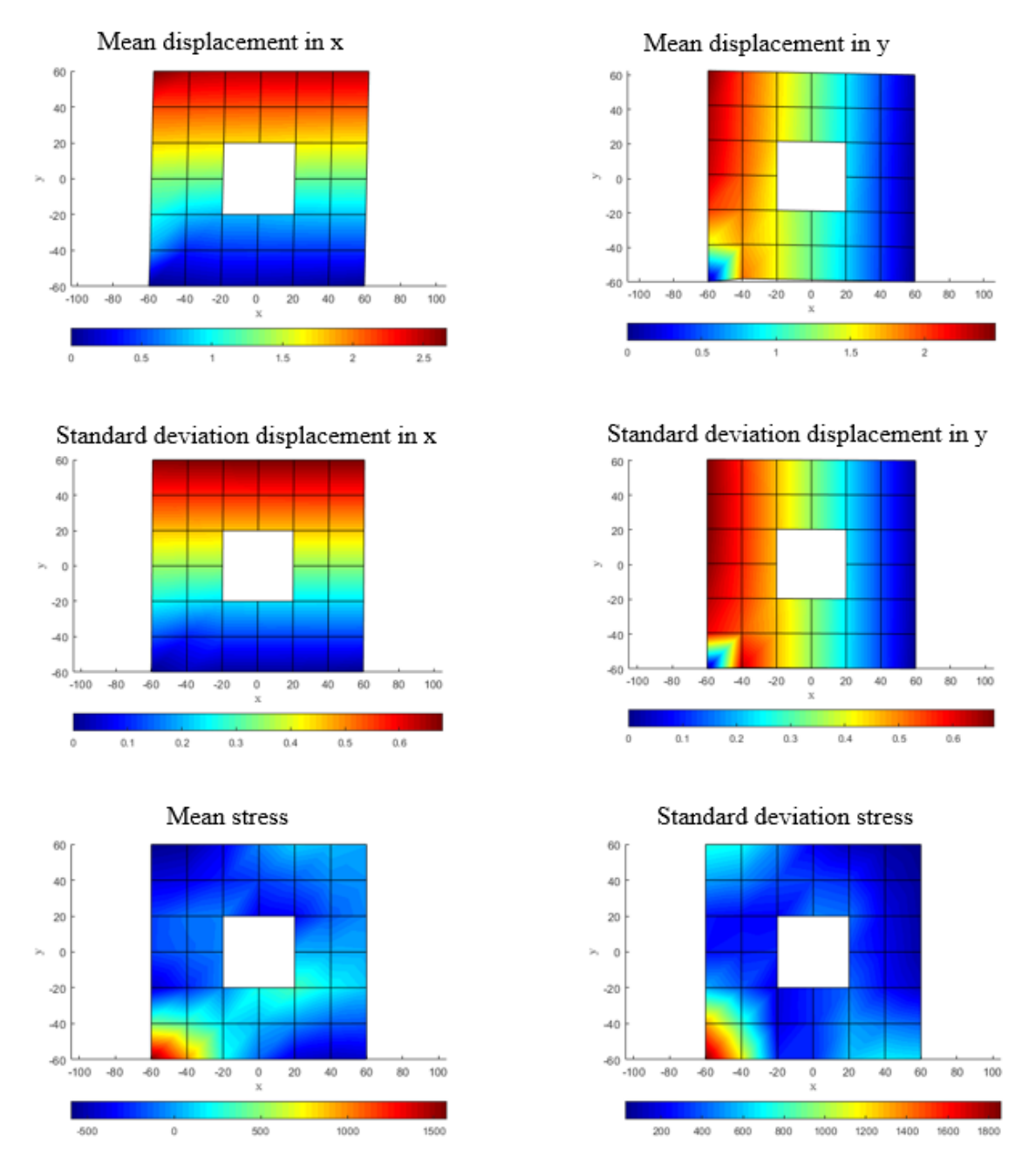
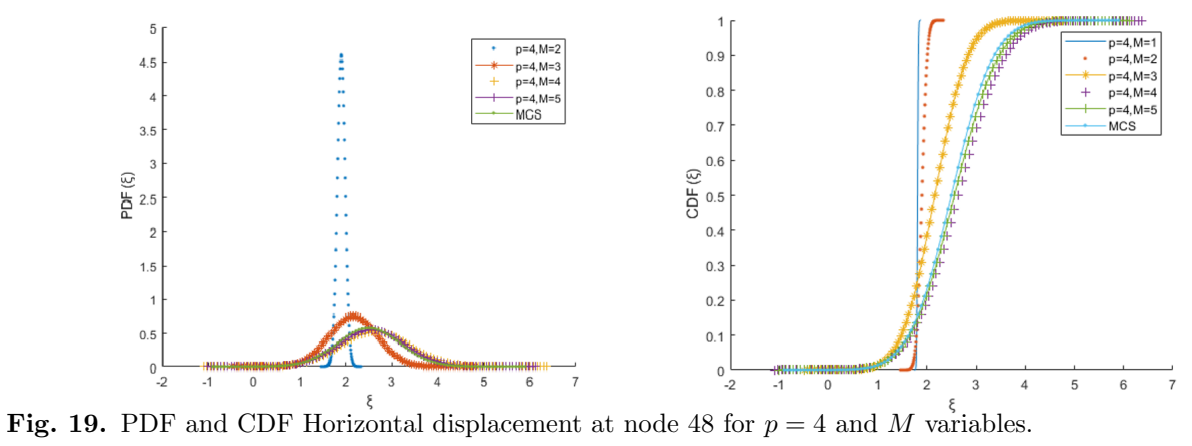


Fig. 18. Mean and standard deviation of displacement and stress in the structure of example 2; Meshing No.



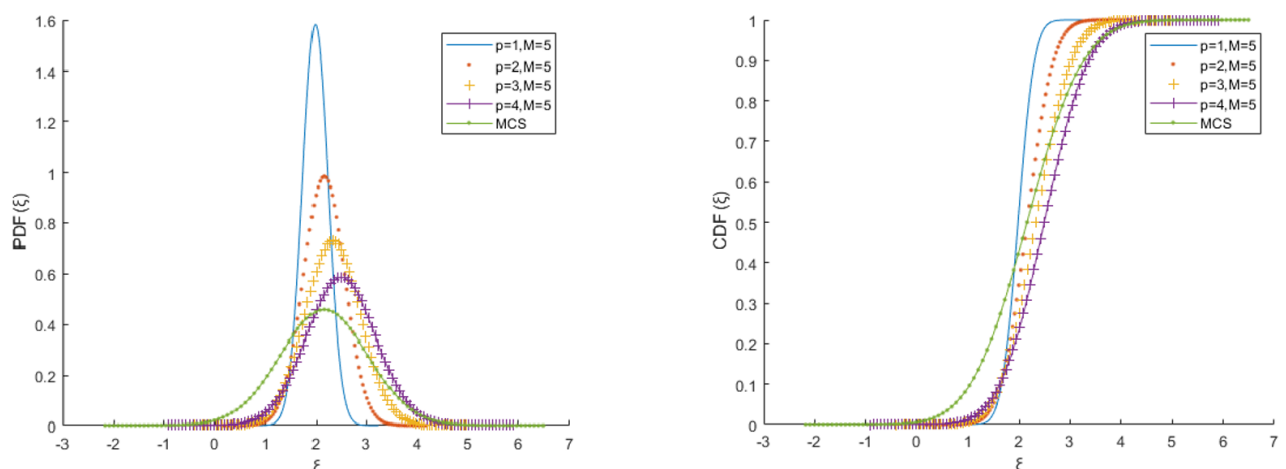


Fig. 20. PDF and CDF of horizontal displacement at node 16 for M=5 and variable p.

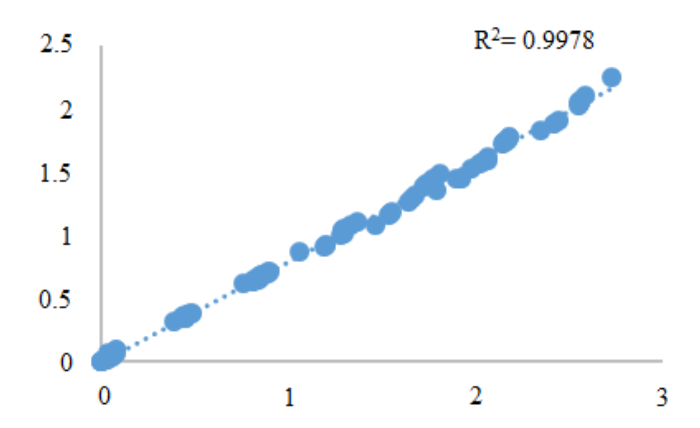


Fig. 21. Correlation between the mean displacement values obtained for meshing 3 of example 2 for the Monte Carlo method and the SSFEM M=4, p=4.

Table 5
Probability of failure and structural analysis time of example 2.

Time (sec)	β	Pf	Case
1375265	3.2835	0.0112	MCS
115421	3.2476	0.0123	NSSFEM

#### 6. Conclusions

Factoring in uncertainty in the structure's input parameters complicates the problem, particularly because nonlinear analysis is both time-consuming and computationally intensive. To address this, we introduced the nonlinear spectral stochastic finite element method (NSSFEM), which generalizes the SSFEM for nonlinear problems. The proposed NSSFEM incorporates uncertainties in both materials and loads, making it applicable to structures modeled with elastoplastic materials. Our modeling results demonstrate that using NSSFEM, as opposed to Monte Carlo Simulation (MCS), significantly reduces the computation time required to obtain structural responses. Additionally,

NSSFEM achieves an error rate of less than 3% in these responses. The proposed NSSFEM was also utilized to analyze the reliability of structures. The values of the Karhunen-Loève expansion (KLE) and polynomial chaos expansion (PCE) terms were optimized. The findings indicate that increasing the number of KLE terms (M) has a greater impact on accuracy than increasing the order of PCE (p). Moreover, both increasing and decreasing KLE terms are more effective in enhancing the result accuracy. This study shows that larger structures require fewer KLE and PCE terms to achieve the desired level of accuracy. Overall, the results from NSSFEM demonstrate 97% accuracy while significantly reducing the computation time.

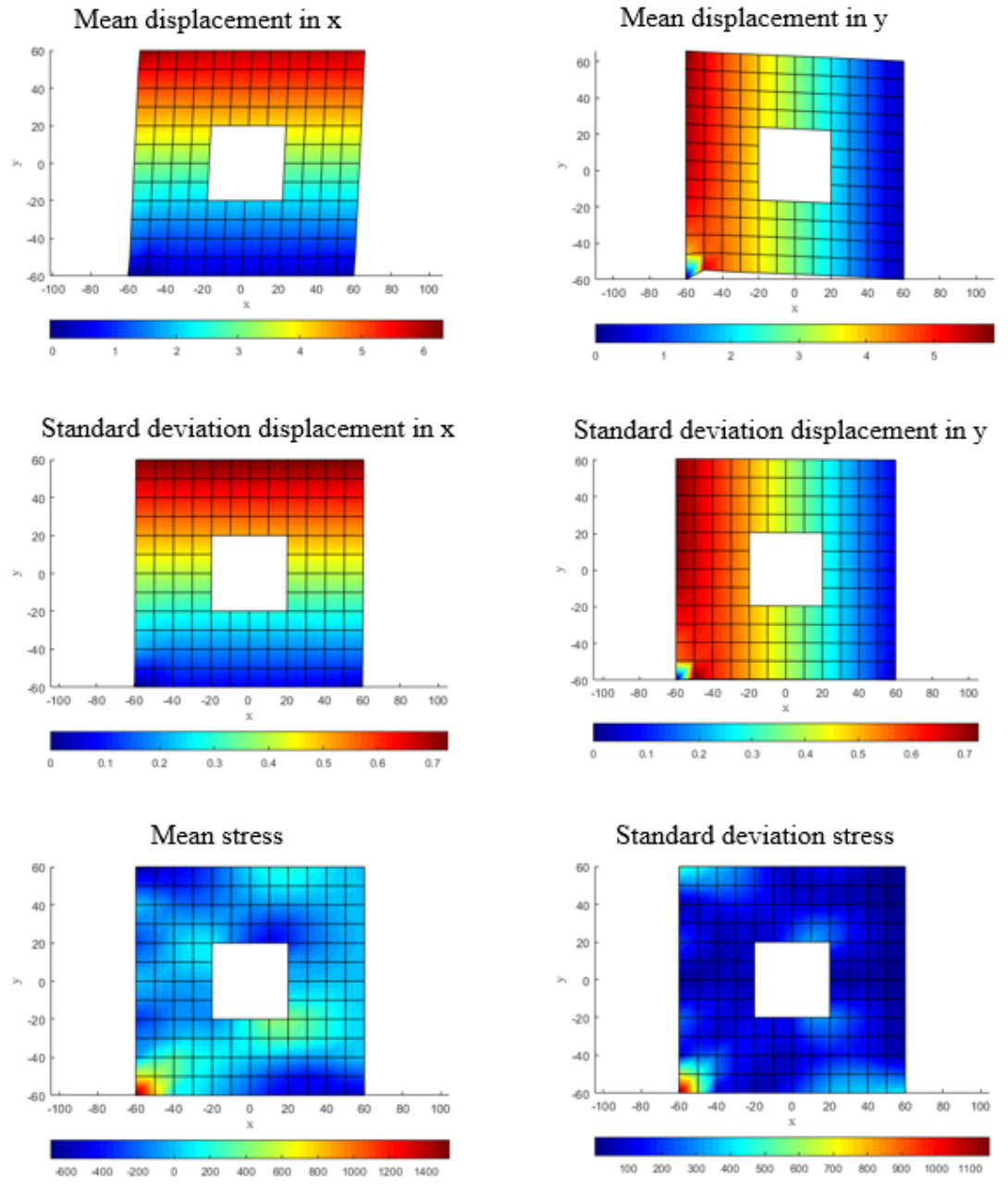


**Fig. 22.** Mean and standard deviation of displacement and stress in the structure of example 2; meshing No. 3.

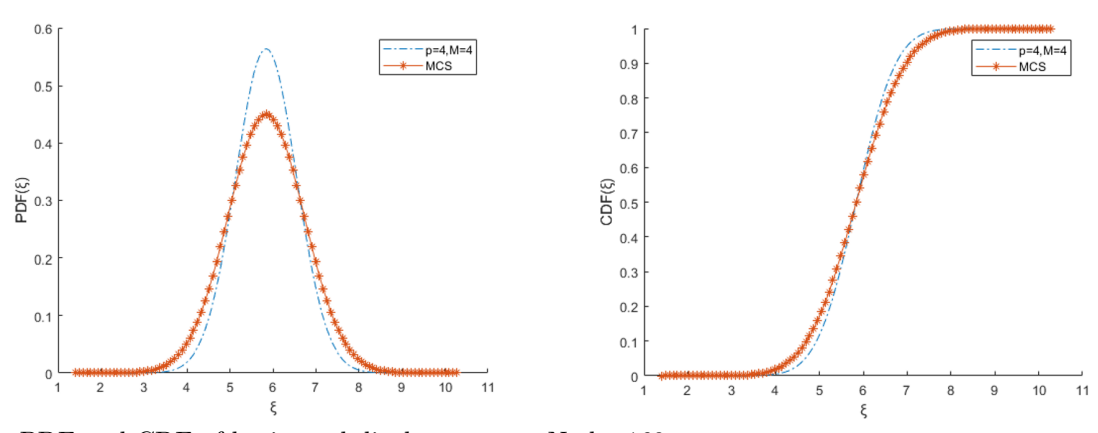
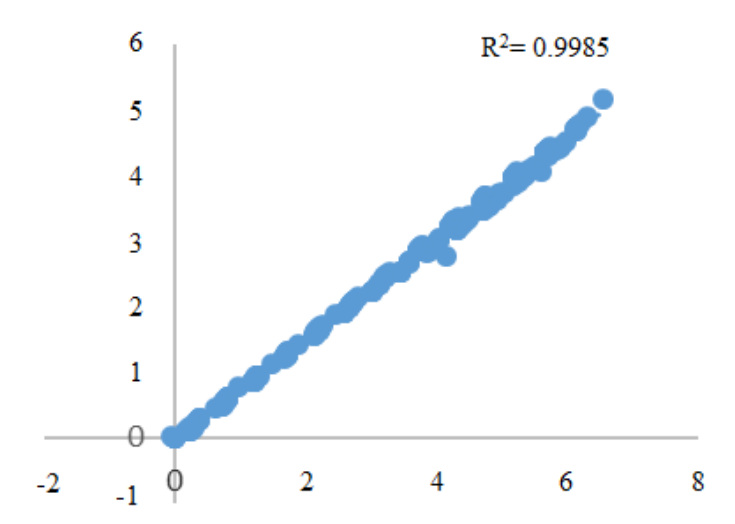


Fig. 23. PDF and CDF of horizontal displacement at Node 160.



**Fig. 24.** Correlation between the mean displacement values obtained for meshing 3 of example 2 for the Monte Carlo method and the SSFEM M = 4, p = 4.

#### References

- Z. Zheng, H. Dai, "Structural stochastic responses determination via a sample-based stochastic finite element method," Comput. Methods Appl. Mech. Eng., vol. 381, (2021), doi: 10.1016/j.cma.2021.113824.
- [2] M.R. Machado, S. Adhikari, J.M.C. Dos Santos, "A spectral approach for damage quantification in stochastic dynamic systems," Mech. Syst. Signal Process., 88 (2017) 253-273, doi: 10.1016/j.ymssp.2016.11.018.
- [3] D.E.M. Bouhjiti, J. Baroth, F. Dufour, S. Michel-Ponnelle, and B. Masson, "Stochastic finite elements analysis of large concrete structures' serviceability under thermo-hydromechanical loads-Case of nuclear containment buildings," Nucl. Eng. Des., 370 (2020), doi: 10.1016/j.nucengdes.2020.110800.
- [4] F. Wu, K. Chen, T.Y. Wang, L.Y. Yao, M. Hu, "Stochastic hybrid perturbation technique-based smoothed finite element-statistical energy method for mid-frequency analysis of structure–acoustic systems with parametric and non-parametric uncertainties," Comput. Methods Appl. Mech. Eng., 349 (2019) 522-549, doi: 10.1016/j.cma.2019.02.034.
- [5] S. Dutta, S. Ghosh, "Form-finding of framesupported tensile membrane structures using stochastic optimisation," Structures, 32 (2021) 2211-2221, doi: 10.1016/j.istruc.2021.03.103.
- [6] S. Shang, G.J. Yun, "Stochastic finite element with material uncertainties: Implementation in a general purpose simulation program,"

- Finite Elem. Anal. Des., 64 (2013) 65-78, doi: 10.1016/j.finel.2012.10.001.
- [7] P. Zakian, N. Khaji, "A novel stochastic-spectral finite element method for analysis of elastodynamic problems in the time domain," Meccanica, 51(4) (2016) 893-920, doi: 10.1007/s11012-015-0242-9.
- [8] F. Bouchoucha, M.N. Ichchou, M. Haddar, "Diffusion matrix through stochastic wave finite element method," Finite Elem. Anal. Des., 64 (2013) 97-107, doi: 10.1016/j.finel.2012.09.008.
- [9] G.E. Zouraris, I. Babuška, R. Tempone, "Galerkin finite element approximations of stochastic elliptic partial differential equations," SIAM J. Numer. Anal., 42(2) (2004) 800-825, [Online]. Available: http://epubs.siam.org/doi/abs/10.1137/S00361 42902418680.
- [10] Y.P. Liang, X. Ren, D.C. Feng, "Efficient stochastic finite element analysis of irregular wall structures with inelastic random field properties over manifold," Comput. Mech., (2021) 1-17, doi: 10.1007/s00466-021-02084-4.
- [11] G. Stefanou, M. Papadrakakis, "Stochastic finite element analysis of shells with combined random material and geometric properties," Comput. Methods Appl. Mech. Eng., vol. 193(1-2) (2004) 139-160, doi: 10.1016/j.cma.2003.10.001.
- [12] M.F. Ngah, A. Young, "Application of the spectral stochastic finite element method for performance prediction of composite structures," Compos. Struct., 78(3) (2007) 447-456, doi: 10.1016/j.compstruct.2005.11.009.

- [13] A. Yazdani, H. Ghohani Arab, M. Rashki, "Simplified spectral stochastic finite element formulations for uncertainty quantification of engineering structures," Structures, 28 (2020) 1924-1945, doi: 10.1016/j.istruc.2020.09.040.
- [14] G. Stefanou, "The stochastic finite element method: Past, present and future," Comput. Methods Appl. Mech. Eng., 198(9-12) (2009) 1031-1051, doi: 10.1016/j.cma.2008.11.007.
- [15] R.G. Ghanem, P.D. Spanos, Stochastic Finite Elements: A Spectral Approach. Courier Dover Publications, (1991). doi: 10.1007/978-1-4612-3094-6.
- [16] D.G.G. Vissarion Papadopoulos, Stochastic Finite Element Methods. Springer, (2018).
- [17] H. Huo, W. Xu, W. Wang, G. Chen. D. Yang, "New non-intrusive stochastic finite element method for plate structures," Comput. Struct., 268 (2022),10.1016/j.compstruc.2022.106812.
- [18] M. Anders, M. Hori, "Stochastic finite element method for elasto-plastic body,"
  Int. J. Numer. Methods Eng., 46 (11) (1999) 1897-1916, doi: 10.1002/(SICI)1097-0207(19991220)46:11;1897::AID-NME758;3.0.CO;2-3.
- [19] G. Stavroulakis, D.G. Giovanis, V. apadopoulos, M. Papadrakakis, "A GPU domain decomposition solution for spectral stochastic finite element method," Solut. Spectr. Stoch. finite Elem. method, 327, (2017) 392-410.
- [20] K. Sepahvand, S. Marburg, "Spectral stochastic finite element method in vibroacoustic analysis of fiber-reinforced composites," Procedia Eng., 199 (2017) 1134-1139, doi: 10.1016/j.proeng.2017.09.241.
- [21] Y. Appalanaidu, A. Roy, S. Gupta, "Stochastic creep damage estimation in pipings with spatial non-Gaussian uncertainties using spectral stochastic finite element method," Procedia Eng., 86 (2014) 677-684, doi: 10.1016/j.proeng.2014.11.069.
- [22] R.G. Ghanem, P.D. Spanos, Stochastic Finite Element Method: Response Statistics. Springer, (1991). doi: 10.1007/978-1-4612-3094-6\_4.
- [23] R.G. Ghanem, P.D. Spanos, "Spectral techniques for stochastic finite elements," Arch. Comput. Methods Eng., 4(1) (1997) 63-100, doi: 10.1007/BF02818931.

- [24] S. Zhang, X. Guan, L. Jiang, "Convergence analysis of constraint energy minimizing generalized multiscale finite element method for a linear stochastic parabolic partial differential equation driven by additive noises," J. Comput. Appl. Math., 389 (2021), doi: 10.1016/j.cam.2020.113328.
- [25] J. Schröder, D. Balzani, D. Brands, "Approximation of random microstructures by periodic statistically similar representative volume elements based on lineal-path functions," Arch. Appl. Mech., 81(7) (2011) 975-997, doi: 10.1007/s00419-010-0462-3.
- [26] A. Shaker, W.G. Abdelrahman, M. Tawfik, E. Sadek, "Stochastic finite element analysis of the free vibration of laminated composite plates," Comput. Mech., 41(4) (2008) 493-501, doi: 10.1007/s00466-007-0205-7.
- [27] M. Nadjafi, P. Gholami, "Reliability Study of Notched Composite Laminates Under Uniaxial Loading Based on Continuum Damage Mechanics Approach," Iran. J. Sci. Technol. Trans. Mech. Eng., (2021), doi: 10.1007/s40997-021-00458-w.
- [28] E. Bahmyari, "Stochastic Vibration Analysis of Laminated Composite Plates with Elastically Restrained Edges Using the Non-Intrusive Chaotic Radial Basis Function," Iran. J. Sci. Technol. -Trans. Mech. Eng., (2022), doi: 10.1007/s40997-022-00511-2.
- [29] A. Mouyeaux, C. Carvajal, P. Bressolette, L. Peyras, P. Breul, C. Bacconnet, "Probabilistic stability analysis of an earth dam by Stochastic Finite Element Method based on field data," Comput. Geotech., 101 (2018) 34-47, doi: 10.1016/j.compgeo.2018.04.017.
- [30] M. Kamiński, P. Świta, "Structural stability and reliability of the underground steel tanks with the Stochastic Finite Element Method," Arch. Civ. Mech. Eng., 15(2) (2015) 593-602, doi: 10.1016/j.acme.2014.04.010.
- [31] J. Füssl, G. Kandler, J. Eberhardsteiner, "Application of stochastic finite element approaches to wood-based products," Arch. Appl. Mech., 86(1-2)(2016) 89-110, doi: 10.1007/s00419-015-1112-6.
- [32] M. Lacour, J. Macedo, and N. A. Abrahamson, "Stochastic finite element method for non-linear material models," Comput. Geotech., 125 (2020), doi: 10.1016/j.compgeo.2020.103641.
- [33] C.K. Nowak AS, Reliability of structures. CRC Press, (2013).

- [34] B. Sudret, A. Der Kiureghian, Stochastic Finite Element Methods and Reliability, no. October. (2000).
- [35] C.H. Ma, J. Yang, L. Cheng, L. Ran, "Research on slope reliability analysis using multi-kernel relevance vector machine and advanced first-order second-moment method," Eng. Comput., (2021), doi: 10.1007/s00366-021-01331-9.
- [36] R. Ghanem, G. Saad, A. Doostan, "Efficient solution of stochastic systems: Application to the embankment dam problem," Struct. Saf., 29(3) (2007) 238–251, doi: 10.1016/j.strusafe.2006.07.015.
- [37] P. Zakian, N. Khaji, A. Kaveh, "Graph theoretical methods for efficient stochastic finite element analysis of structures," Comput. Struct., 178 (2017) 29-46, doi: 10.1016/j.compstruc.2016.10.009.
- [38] S.E. Pryse, S. Adhikari, "Neumann enriched polynomial chaos approach for stochastic finite element problems," Probabilistic Eng. Mech., 66 (2021), doi: 10.1016/j.probengmech.2021.103157.
- [39] W.F. Chen, D.J. Han, Plasticity for Structural Engineers. Springer, (1988). doi: 10.1007/978-1-4612-3864-5.

- [40] R. De Borst, M.A. Crisfield, J.J. Remmers, C.V. Verhoosel, Non-Linear Finite Element Analysis of Solids and Structures: Second Edition. JOHN WILEY & SONS, (2012). doi: 10.1002/9781118375938.
- [41] K.J. Bathe, Finite Element Procedures. Prentice-Hall, (2005). [Online]. Available: http://books.google.com/books?id=wKRRAAAA MAAJ&pgis=1%5 Cn-ftp://ftp.demec.ufpr.br/disciplinas/EME748/ Textos/Bathe, K.-J. Finite Element Procedures 1996 Prentice-Hall ISBN 0133014584 1052s.pdf
- [42] J. Huang, D.V. Griffiths, "Return mapping algorithms and stress predictors for failure analysis in geomechanics," J. Eng. Mech., 135(4) (2009) 276-284, doi: 10.1061/(asce)0733-9399(2009)135:4(276).
- [43] S. Im, J. Lee, M. Cho, "Surrogate modeling of elasto-plastic problems via long short-term memory neural networks and proper orthogonal decomposition," Comput. Methods Appl. Mech. Eng., 385 (2021), doi: 10.1016/j.cma.2021.114030.